



HAL
open science

A class of fluid-structure interaction problems with analytical solutions

Yongxing Wang, Olivier Pironneau

► **To cite this version:**

Yongxing Wang, Olivier Pironneau. A class of fluid-structure interaction problems with analytical solutions. International Journal for Numerical Methods in Engineering, In press. hal-04580186v2

HAL Id: hal-04580186

<https://hal.science/hal-04580186v2>

Submitted on 27 May 2024

HAL is a multi-disciplinary open access archive for the deposit and dissemination of scientific research documents, whether they are published or not. The documents may come from teaching and research institutions in France or abroad, or from public or private research centers.

L'archive ouverte pluridisciplinaire **HAL**, est destinée au dépôt et à la diffusion de documents scientifiques de niveau recherche, publiés ou non, émanant des établissements d'enseignement et de recherche français ou étrangers, des laboratoires publics ou privés.

A class of fluid-structure interaction problems with analytical solutions

Yongxing Wang^{a,*}, Olivier Pironneau^b

^a*School of Computing, University of Leeds, Leeds, UK.*

^b*LJLL, Sorbonne Université, Paris, France*

Abstract

Analytical solutions to Fluid-Structure Interaction (FSI) problems are almost absent in the literature. However, they are not only essential for understanding the intricate coupling dynamics between fluids and solids, but they also serve as benchmarks for validating and analysing the convergence of numerical algorithms. In this paper, we derive two analytical and one semi-analytical solutions for three FSI problems, spanning a class of solutions by varying their geometrical and physical parameters. All solutions exhibit complex nonlinear behaviours, which we validate through numerical simulations using a monolithic method. These three FSI problems are described in the cylindrical coordinates, drawing inspiration from Couette flow, with two of them featuring a moving fluid-solid interface and the third incorporating a nonlinear constitutive solid model. To the best of our knowledge, for the first time, we present FSI problems with analytical solutions that include a moving interface.

Keywords: Fluid-structure interaction, Analytical solution, Finite element, Monolithic method, One-velocity field

1. Introduction

Fluid-Structure Interaction (FSI) problems are prevalent across various fields, including aerodynamics [1–4], biomedical science [2, 5–7], ocean dynamics [8–11], and so on. For most FSI problems, analytical solutions of the controlling equations are impossible to obtain, whereas laboratory experiments are complex, expensive, and limited in scope. Therefore, numerical simulations play an important role in order to understand the fundamental physics involved in the complex interaction between fluids and structures.

1.1. A brief summary of numerical methods for fluid-structure interactions

Numerical methods for FSI problems have rapidly advanced over recent decades. Classical partitioned or segregated methods, as referenced in [2, 12–30], have been prominent over the past two decades. These methods utilise a single interface-fitted mesh to solve

*Corresponding author

Email address: `sosywan@leeds.ac.uk` (Yongxing Wang)

for both fluid velocity and solid displacement. These methods represent some of the earliest numerical approaches developed for FSI problems and are still evolving, particularly in terms of parallelisation [24, 28], efficiency [25, 27], stability, accuracy [29], and adaptivity [26, 29, 30]. For two-way coupling (or strong coupling) FSI problems, partitioned methods iteratively solve for the fluid and solid problems separately. They exchange information across the fluid-solid interface until achieving a balance of variables at the interface. The advantage of classical partitioned methods is their relative ease of implementation, often based on the coupling of existing fluid and solid code. However, their drawback lies in the difficulty of guaranteeing convergence during iteration, especially when there is rapid energy exchange between the fluid and solid at the interface [19, 20]. A simplified version of these two-way partitioned methods is the one-way FSI method. In this method, only the fluid problem is solved explicitly, while the solid deforms passively by following the fluid fields. It provides an updated boundary condition for the fluid problem for every time frame [31–33].

Monolithic methods were developed to overcome the limitations of partitioned methods, which solve the fluid and solid equations within a single equation system. This approach has gained widespread acceptance as a more robust numerical method compared to classic partitioned methods. Initially, monolithic methods were based on an ALE interface-fitted mesh. They solve for fluid velocity, pressure, solid displacement, and use a Lagrange multiplier to enforce continuity at the fluid-solid interface [7, 34–36].

Recent advancements in monolithic methods have introduced the use of a background Cartesian grid with locally cut triangles to accommodate the fluid-solid interface, named as the locally modified FEM [37–40]. This method solves for the variables of fluid velocity and pressure, as well as solid displacement or velocity. In comparison to traditional ALE methods, it circumvents the need for a moving mesh and is proficient in handling arbitrarily large solid deformations. However, a difficulty lies in the management of local anisotropic FEM mesh—Edge stabilisation techniques [41] are introduced to enhance the stability.

Monolithic methods have also evolved to use two meshes [42–44]. This approach addresses fluid velocity, pressure, and solid displacement while using a distributed Lagrange multiplier to ensure velocity consistency between the meshes. Another variation is the cutFEM-based FSI method [45, 46], which extends the solid foreground mesh to envelop a surrounding artificial fluid mesh with a fitted interface. This method involves cutting through local elements around the interface for numerical quadrature without modifying local degrees of freedom, unlike the locally modified method. However, stability issues arise due to possible irregularities in local meshes, leading to the adoption of Nitsche-type interface coupling strategies with ghost penalty terms [47] to guarantee stability. The initial version of this cutFEM-based approach was presented in [48] as a partitioned approach.

Alternatively, monolithic methods have been adapted to employ a single mesh without interface fitting, known as the fully Eulerian formulation [49–55]. These methods use an Initial Points (IP) set to capture the fluid-structure interface, extending the unknown variables across the entire domain with a characteristic function. The FSI system is solved in a monolithic manner.

Recently, we developed a one-velocity method that solves for a single velocity field across the entire FSI domain, using either a single interface-fitted mesh [56–59] or two meshes [60–

63]. In this one-velocity method, the solid equations are first expressed in terms of velocity, automatically ensuring velocity consistency at the fluid-solid interface with one interface-fitted mesh. When using two meshes, finite element isoparametric interpolation is employed to maintain velocity consistency. We shall benchmark this one-velocity monolithic method against the three (semi-)analytical FSI problems proposed in this paper.

1.2. Analytical solutions in special computational domains

Analytical solutions to the Navier-Stokes equation may only be obtained for simple geometries with additional assumptions, utilising symmetry to reduce the equation to lower dimensions, such as the Couette flow between two concentric cylinders [64, 65], or the pulsatile flow in a pipe [66]. Both the Couette flow and the pulsatile flow can be modelled in a cylindrical coordinate system: $r - \theta - z$ are radial, circumferential, and axial coordinates respectively as shown in Figure 1; exploring the symmetry, the former may be reduced to a problem on $r - \theta$ plane while the latter on $r - z$ plane. Additional assumptions of the velocity profiles of the Couette and the pulsatile flow can further reduce them to one-dimensional problems, which may be solved analytically.

Analytical solutions of FSI problems, where Navier-Stokes equations are coupled with solid equations, have rarely been studied. Building on the Couette and pulsatile fluid flow, analytical FSI problems may be created to fill this gap in the FSI community. In a recent study [67], analytical solutions of the pulsatile flow in an elastic pipe have been derived, which is reduced to a one-dimensional ODE based on the assumption that the fluid velocity and solid displacement are axisymmetric and axially invariant – reduced to a 2D problem on $r - z$ plane, which only have the axial components. In this paper, we consider the Couette flow around an elastic solid as shown in Figure 1, and also assume that the fluid velocity and solid displacement are axisymmetric and axially invariant – reduced to a 2D problem on $r - \theta$ plane. However, depending on the boundary conditions, the velocity and displacement fields have either the radial or circumferential component: Problem II and III respectively in Figure 2 (b). Similar to Couette flow between two parallel plates, we will also consider an FSI problem between two parallel plates (Problem I) as shown in Figure 2 (a). Notice that it is also possible to consider an analytical FSI problem by applying a shearing boundary condition as shown in Figure 2 (a), in which case both the velocity and displacement fields only have components in the vertical direction. However, a very similar scenario has been studied in [67] albeit using the pulsatile-flow boundary conditions applied at the inlet and outlet. Therefore, we shall not consider this case in the current paper and readers may refer to [67] for the corresponding analysis.

The rest of this paper is organised as follows: the partial differential equations of the FSI problems are introduced in Section 2, followed by a discussion of the three FSI problems in Sections 3, 4, and 5 respectively. In each of these sections, the FSI problem is described first, followed by a detailed analysis and derivation of its analytical solution, with numerical validation provided finally. Conclusions are drawn in Section 6.

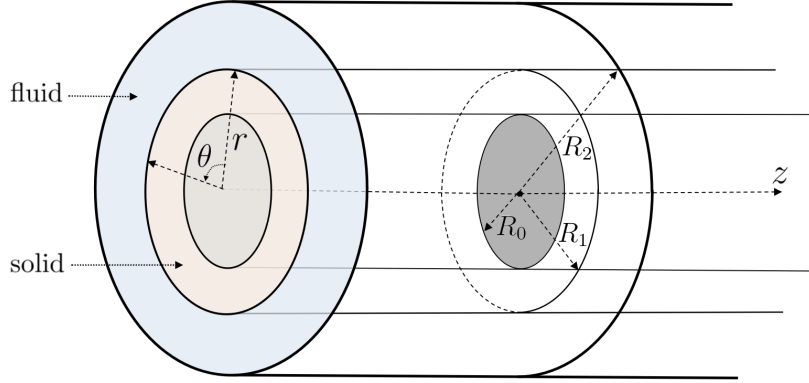


Figure 1: FSI diagram of an elastic solid and viscous fluid between concentric cylinders (R_0 and R_2) with a fixed-rod being the middle cylinder.

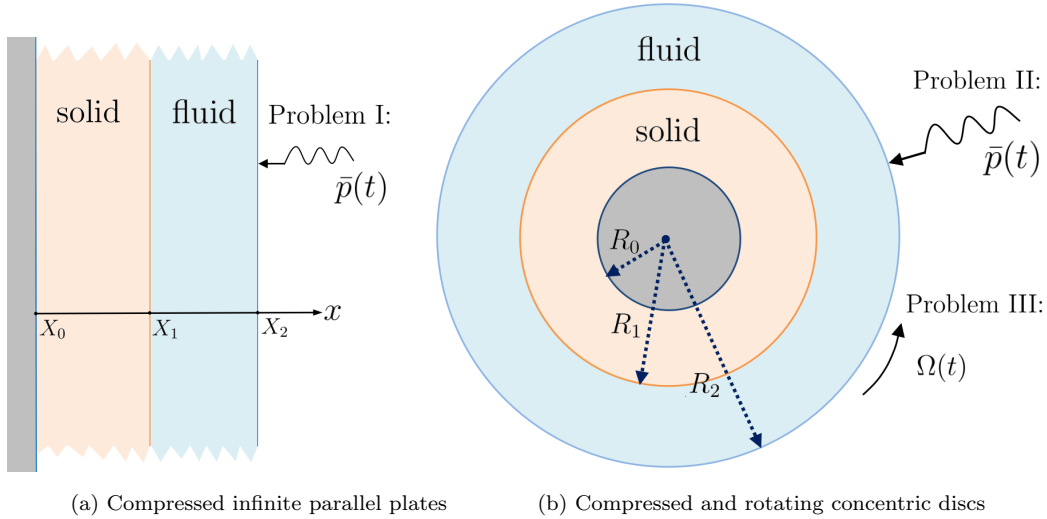


Figure 2: In problem I and II, a periodic normal stress is enforced at outer fluid boundaries, compressing the solids due to the compression of the fluids. In problem III, a periodic circumferential velocity is prescribed at the outer fluid boundary, causing the solid disc to rotate forward and backward due to the rotating fluid.

2. FSI equations

95 In this section, we introduce the partial differential equations for the three fluid-structure interaction problems as illustrated in Figure 2. For the first two cases, a periodic normal force is prescribed at the outer boundary of the fluid, as depicted, causing the solid to be propelled by the fluid and move along the normal/radial direction. For the third case, a periodic velocity is prescribed at the outer boundary of the fluid along the circumferential direction, leading to the solid being dragged to rotate forward and backward.
100

An incompressible Newtonian fluid is utilised for all the three problems in this paper, described as:

$$\rho^f \dot{\mathbf{u}} = \mu^f \nabla \cdot \nabla \mathbf{u} - \nabla p^f, \quad (1)$$

$$\nabla \cdot \mathbf{u} = 0, \quad (2)$$

Where \mathbf{u} represents the velocity vector and p^f denotes the pressure, with ρ^f and μ^f representing the fluid density and viscosity parameters respectively. $\dot{\mathbf{u}} = \frac{d}{dt}\mathbf{u} = \partial_t\mathbf{u} + \mathbf{u} \cdot \nabla\mathbf{u}$ is the total derivative of time.

Two solid models are considered in this paper. In problem I and II, we employ a compressible linear elastic solid described in the reference configuration:

$$\rho^s \ddot{\mathbf{d}} = \mu^s \hat{\nabla} \cdot \left(\hat{\nabla}^\top \mathbf{d} + \hat{\nabla} \mathbf{d} \right) + \lambda^s \hat{\nabla} (\hat{\nabla} \cdot \mathbf{d}), \quad (3)$$

where μ^s and λ^s are the Lamé constants, ρ^s is the solid density, and \mathbf{d} is the displacement vector. In problem III, we use an incompressible hyperelastic neo-Hookean model described in the current configuration:

$$\rho^s \ddot{\mathbf{d}} = \mu^s \nabla \cdot (\mathbf{F}\mathbf{F}^\top - \mathbf{I}) - \nabla p^s. \quad (4)$$

In the above equations (3) and (4), $\ddot{\mathbf{d}} = \frac{d^2}{dt^2}\mathbf{d}$ represents the second-order material derivative with respect to time. The FSI system can be closed by appropriate boundary and initial conditions. As shown in the Figure 2, we shall use a wall-boundary at X_0 or R_0 for all the three problems. At the outer fluid boundary, either a normal stress (Problem I and II) or a tangential velocity profile is prescribed. At the fluid-solid interface (X_1 or R_1), the continuity of the velocity and the continuity of the normal stress are applied. We shall discuss details of these boundary conditions, as well as the initial conditions, separately for the three specific problems in the following sections.

In the above, ∇ and $\hat{\nabla}$ represent the Nabla operator in the current and reference configurations respectively. Equations (1) to (3) do not specify a coordinate system. In the Cartesian coordinate system, we use $X\mathbf{i} + Y\mathbf{j}$ to denote a vector in the reference configuration, and $x\mathbf{i} + y\mathbf{j}$ to denote a vector in the current configuration, with $\mathbf{i} = (1, 0)^\top$ and $\mathbf{j} = (0, 1)^\top$ being the basis vectors. In the polar coordinate system, we use $r\mathbf{e}_r$ and $R\hat{\mathbf{e}}_r$ to represent vectors in the current and reference configurations respectively. The polar basis vectors $\mathbf{e}_r - \mathbf{e}_\theta$ (or $\hat{\mathbf{e}}_r - \hat{\mathbf{e}}_\theta$) are functions of θ (or $\hat{\theta}$) and can be derived as follows: since $(x, y) = (r \cos \theta, r \sin \theta)$,

$$\mathbf{e}_r = \frac{\partial_r(x, y)}{|\partial_r(x, y)|} = (\cos \theta, \sin \theta)^\top, \quad \mathbf{e}_\theta = \frac{\partial_\theta(x, y)}{|\partial_\theta(x, y)|} = (-\sin \theta, \cos \theta)^\top. \quad (5)$$

Similarly, $\hat{\mathbf{e}}_r = (\cos \hat{\theta}, \sin \hat{\theta})^\top$ and $\hat{\mathbf{e}}_\theta = (-\sin \hat{\theta}, \cos \hat{\theta})^\top$. The relation between $(\mathbf{e}_r, \mathbf{e}_\theta)$ and $(\hat{\mathbf{e}}_r, \hat{\mathbf{e}}_\theta)$ is

$$\hat{\mathbf{e}}_r = \cos \alpha \mathbf{e}_r - \sin \alpha \mathbf{e}_\theta, \quad \hat{\mathbf{e}}_\theta = \sin \alpha \mathbf{e}_r + \cos \alpha \mathbf{e}_\theta, \quad (6)$$

where $\alpha = \theta - \hat{\theta}$ is the angular displacement.

It can also be observed that the relationship of the bases between these two coordinate systems is given by:

$$(\mathbf{e}_r, \mathbf{e}_\theta) \mathbf{Q} = (\mathbf{i}, \mathbf{j}) \quad (7)$$

where

$$\mathbf{Q} = \begin{pmatrix} \cos \theta & \sin \theta \\ -\sin \theta & \cos \theta \end{pmatrix}. \quad (8)$$

With the above notations, it is straightforward to compute the Jacobi matrix

$$\mathbf{J} = \partial_{(r,\theta)}(x, y) = \begin{pmatrix} \cos \theta & \sin \theta \\ -r \sin \theta & r \cos \theta \end{pmatrix} \quad (9)$$

135 and its inverse

$$\mathbf{J}^{-1} = \partial_{(x,y)}(r, \theta) = \frac{1}{r} \begin{pmatrix} r \cos \theta & -\sin \theta \\ r \sin \theta & \cos \theta \end{pmatrix} \quad (10)$$

and further the Nabla operator in the polar coordinate system:

$$\nabla = (\mathbf{i}, \mathbf{j})\partial_{(x,y)} = (\mathbf{e}_r, \mathbf{e}_\theta) \mathbf{QJ}^{-1}\partial_{(r,\theta)} = \left(\mathbf{e}_r, \frac{\mathbf{e}_\theta}{r} \right) \partial_{(r,\theta)} = \mathbf{e}_r \partial_r + \mathbf{e}_\theta \frac{1}{r} \partial_\theta. \quad (11)$$

The Nabla operator is a first-order tensor. The derivative of the polar basis:

$$\begin{pmatrix} \partial_r \mathbf{e}_r & \partial_r \mathbf{e}_\theta \\ \partial_\theta \mathbf{e}_r & \partial_\theta \mathbf{e}_\theta \end{pmatrix} = \begin{pmatrix} 0 & 0 \\ \mathbf{e}_\theta & -\mathbf{e}_r \end{pmatrix} = \mathbf{e}_\theta (\mathbf{e}_r \mathbf{e}_\theta) - \mathbf{e}_r (\mathbf{e}_\theta \mathbf{e}_\theta) \quad (12)$$

will also be used to derive the control equations in the following sections, which is a second-order tensor, with basis $\mathbf{e}_r \mathbf{e}_\theta$ being $\mathbf{e}_r \otimes \mathbf{e}_\theta$ for short, etc. We can further compute the dot product of two Nabla operators which is a scalar:

$$\nabla \cdot \nabla = \left(\mathbf{e}_r \partial_r + \mathbf{e}_\theta \frac{1}{r} \partial_\theta \right) \cdot \left(\mathbf{e}_r \partial_r + \mathbf{e}_\theta \frac{1}{r} \partial_\theta \right) = \partial_{rr} + \frac{1}{r} \partial_r + \frac{1}{r^2} \partial_{\theta\theta}. \quad (13)$$

Notice that the operators in (11), (12), and (13) take the same form in the reference coordinate system.

Remark 1. *A special feature of applying normal stress (Problem I and II) is the creation of a moving interface, rendering the FSI problem non-trivial and challenging. In contrast, for*
 145 *Problem III and the pulsatile-type FSI problems described in [67], the FSI interface remains stationary. Here, the complexity lies more in the non-linear solid constitutive model.*

Remark 2. *For Problem I and II, although we consider a linear constitutive model for the solid, the linearity is in the reference configuration – highly non-linear if expressed in the current configuration, while the fluid equation is expressed in the current configuration. This*
 150 *inconsistency makes the FSI problems more challenging and interesting.*

3. Problem I: compressed parallel plates

For the computational geometry and normal-force boundary condition shown in Figure 2 (a), we assume that only the horizontal velocity component u is non-zero, which, together with the pressure p , depends only on x and t . The fluid equations (1) and (2) reduce to
 155 one-dimensional PDEs as follows:

$$\rho_f \dot{u}(x, t) = -p'(x, t), \quad (14)$$

$$u'(x, t) = 0, \quad (15)$$

Similarly, we assume the solid displacement only has the horizontal component d , which is a function of X and t . Then the solid equation (3) is reduced to

$$\rho^s \ddot{d}(X, t) = (2\mu^s + \lambda^s) d''(X, t). \quad (16)$$

The fluid equation (14) is expressed in the current or physical domain corresponding to the reference domain $[X_1, X_2]$, while the solid (16) equation is expressed directly in the reference domain $[X_0, X_1]$. We use the Lagrangian mapping to find the current domain for the fluid, i.e., extending the solid displacement $d(X, t)$ ($X \in [X_0, X_1]$) to the displacement of the fluid particles $\xi(X, t)$ ($X \in [X_1, X_2]$), with $\xi(X_1, t) = d(X_1, t)$ at the interface. Let $x_1(t) = X_1 + \xi(X_1, t)$ and $x_2(t) = X_2 + \xi(X_2, t)$, then $x(X, t) = X + \xi(X, t)$ with $X \in [X_1, X_2]$ represents a general point in the current domain $[x_1(t), x_2(t)]$.

The FSI system is completed with the following boundary conditions:

$$d(X_0, t) = 0, \quad (17)$$

$$\dot{d}(X_1, t) = u(x_1(t), t), \quad (18)$$

$$(2\mu^s + \lambda^s) d'(X_1, t) = -p(x_1(t), t), \quad (19)$$

$$p(x_2(t), t) = \bar{p}(t). \quad (20)$$

3.1. Analytical solution

With $\omega = \phi \sqrt{(2\mu^s + \lambda^s)/\rho^s}$,

$$d(X, t) = \frac{a}{\omega} \sin(\phi(X - X_0)) \sin(\omega t), \quad (21)$$

is the general solution of (16), and also satisfies the homogeneous boundary condition (17) and initial condition $d(X, 0) = 0$.

$$\dot{d}(X_1, t) = a \sin(\phi(X_1 - X_0)) \cos(\omega t) \quad (22)$$

is the velocity at the interface and also equivalent to the fluid velocity, $u(x, t)$, across the fluid domain $[X_1, X_2]$, since (15): $u'(x, t) = 0 \Rightarrow u(x, t)$ is constant in x . Therefore, according to (14), the pressure is

$$p'(x, t) = \omega \rho^f a \sin(\phi(X_1 - X_0)) \sin(\omega t), \quad (23)$$

or

$$p(x, t) = p^0(t) + x \omega \rho^f a \sin(\phi(X_1 - X_0)) \sin(\omega t). \quad (24)$$

Matching the normal stresses at the interface (19) gives

$$\begin{aligned} p^0(t) + (X_1 + d(X_1, t)) \omega \rho^f a \sin(\phi(X_1 - X_0)) \sin(\omega t) \\ = - \frac{a \phi (2\mu^s + \lambda^s)}{\omega} \cos(\phi(X_1 - X_0)) \sin(\omega t), \end{aligned} \quad (25)$$

and this equations determines $p^0(t)$:

$$\begin{aligned} p^0(t) = - (X_1 + d(X_1, t)) \omega \rho^f a \sin(\phi(X_1 - X_0)) \sin(\omega t) \\ - \frac{a \phi (2\mu^s + \lambda^s)}{\omega} \cos(\phi(X_1 - X_0)) \sin(\omega t). \end{aligned} \quad (26)$$

Let the initial displacement and velocity be $d(X, 0) = 0$ and $u(x, 0) = a \sin(\phi(X_1 - X_0))$ respectively. Since the fluid velocity, across the whole fluid domain, is the same as the velocity at the interface. By an integration in time, we know that the displacements of the fluid particles $\xi(X, t) = d(X_1, t)$ are independent of X as well. Therefore, $x - x_1(t) = X - X_1$.
180 Based on this relation, the solutions for the FSI equations (14) to (20) are summarised as follows:

$$d(X, t) = \frac{a}{\omega} \sin(\phi(X - X_0)) \sin(\omega t), \quad X \in [X_0, X_1]. \quad (27)$$

$$p(x(X, t), t) = \left[(X - X_1) \omega \rho^f a \sin(\phi(X_1 - X_0)) - \frac{a \phi(2\mu^s + \lambda^s)}{\omega} \cos(\phi(X_1 - X_0)) \right] \sin(\omega t), \quad (28)$$

$$u(x, t) = a \sin(\phi(X_1 - X_0)) \cos(\omega t), \quad x \in [X_1, X_2]. \quad (29)$$

The motion of the interface is included in the solution $d(X, t)$, i.e.: $X_1 + d(X_1, t)$. The
185 boundary pressure is also included in the solution as:

$$\begin{aligned} \bar{p}(t) &= p(x_2(t), t) \\ &= \left[(X_2 - X_1) \omega \rho^f a \sin(\phi(X_1 - X_0)) - \frac{a \phi(2\mu^s + \lambda^s)}{\omega} \cos(\phi(X_1 - X_0)) \right] \sin(\omega t), \end{aligned} \quad (30)$$

which is periodic in time with a frequency of ω .

3.2. Numerical validation

In this section we validate the analytical solutions derived in the previous section, using the one-velocity FSI method as described in Appendix A. The implementation is based on
190 FreeFem++ [68], using the parameter set in Table 1 as an example, for which the maximal solid displacement is around 5% = 0.05/($X_1 - X_0$) of the width of the solid domain.

Remark 3. *The analytical solutions (27), (28), and (29) hold for solid deformations larger than 5%, despite Lamé's equation (3) assuming small displacements in physics. However, the numerical simulation becomes challenging due the moving mesh, and also because one has
195 to make sure the vertical components of the velocity and displacement are always numerically negligible.*

ρ^f	ρ^s	μ^f	μ^s	λ^s	X_0	X_1	X_2	ϕ	a
1	2	2	10	100	3	4	5	1.75π	2

Table 1: A group of parameters for the compressed parallel plates.

We consider computation domain of a $\Omega_1 = (X_2 - X_0) \times H = 2 \times 4$ rectangle and apply a periodic boundary at the top and bottom boundaries. We start from a relative coarse mesh with 861 nodes and 1600 triangles as shown in Figure 3, and a time step of $\Delta t = 10^{-3}$
200 to compute up to a time of $T_1 = 0.5$ which is more than 3 time periods of oscillations.

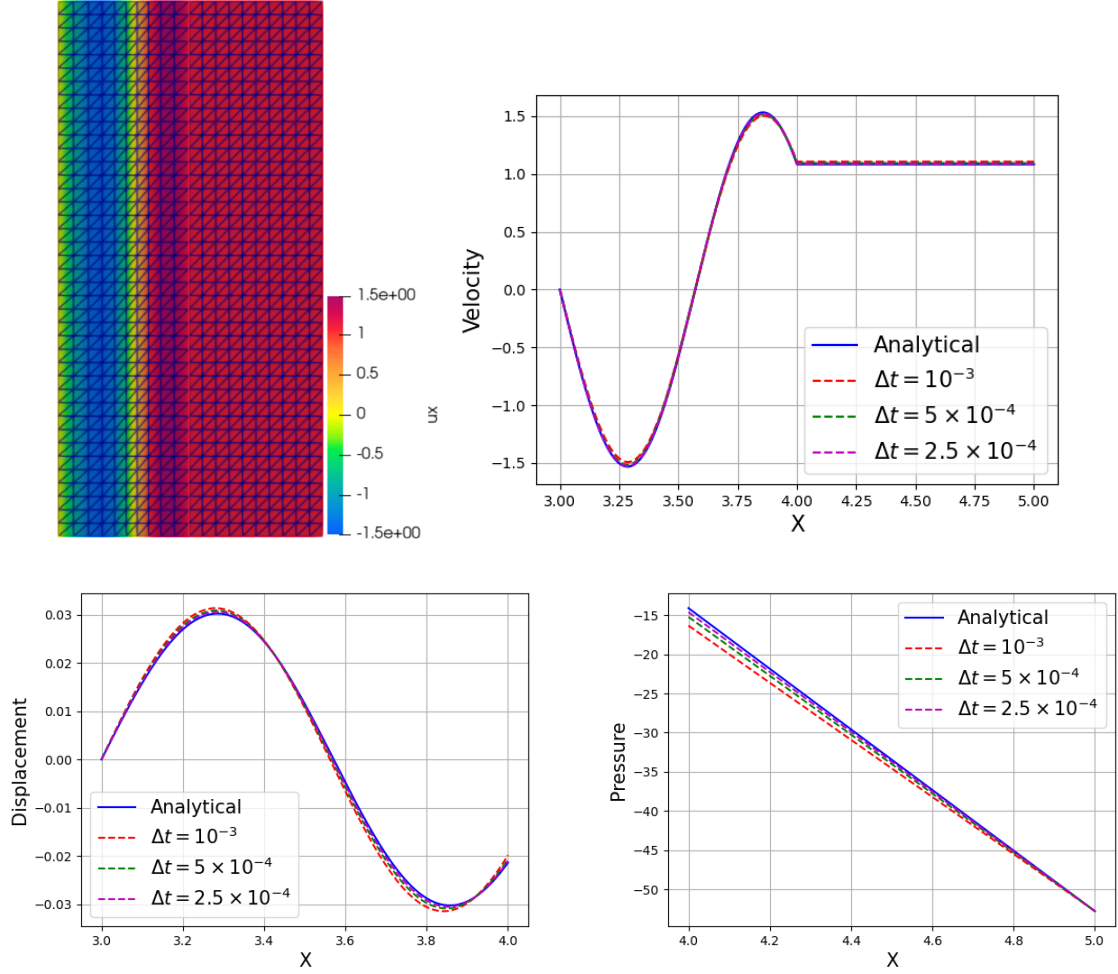


Figure 3: Diagram showing the numerical result as well as its comparison with the analytical solutions at $t = 0.5$: from left to right and top to bottom, horizontal velocity on a coarse mesh, comparisons of the velocity, displacement and pressure.

All the numerical results of velocity, pressure and displacement already agree well with our analytical solutions on this coarse mesh as shown in Figure 3, although we observe that the errors increase gradually as time evolves.

Based on the coarse mesh (Figure 3) and $\Delta t = 10^{-3}$, we refine the mesh and reduce the time step to test the spatiotemporal convergence of the numerical methods using $L^2([0, T_1]; L^2(\Omega_1))$ norm: first compute the $L^2(\Omega_1)$ error given a specific time, denoted by $e(t)$, then compute $L^2([0, T_1])$ norm of $e(t)$. We use a backward Euler scheme for the time discretisation and P_2P_1 element for the space discretisation of the velocity-pressure pair. The optimal spatiotemporal convergence is achieved as shown in Figure 4.

Remark 4. *There is a special case when $\phi(X_1 - X_0) = n\pi$ with $n \in \mathbb{N}$, in which $u(x, t) \equiv 0$. This means the entire fluid remains stationary, while a compressed solid wave oscillates across $[X_0, X_1]$, with the boundary pressure $\bar{p}(t)$ passing through the fluid and directly acting on the solid. Please refer to Appendix Appendix B.1 for a brief test of this case and the supporting animations at <https://yongxingwang.github.io/simulation/>.*

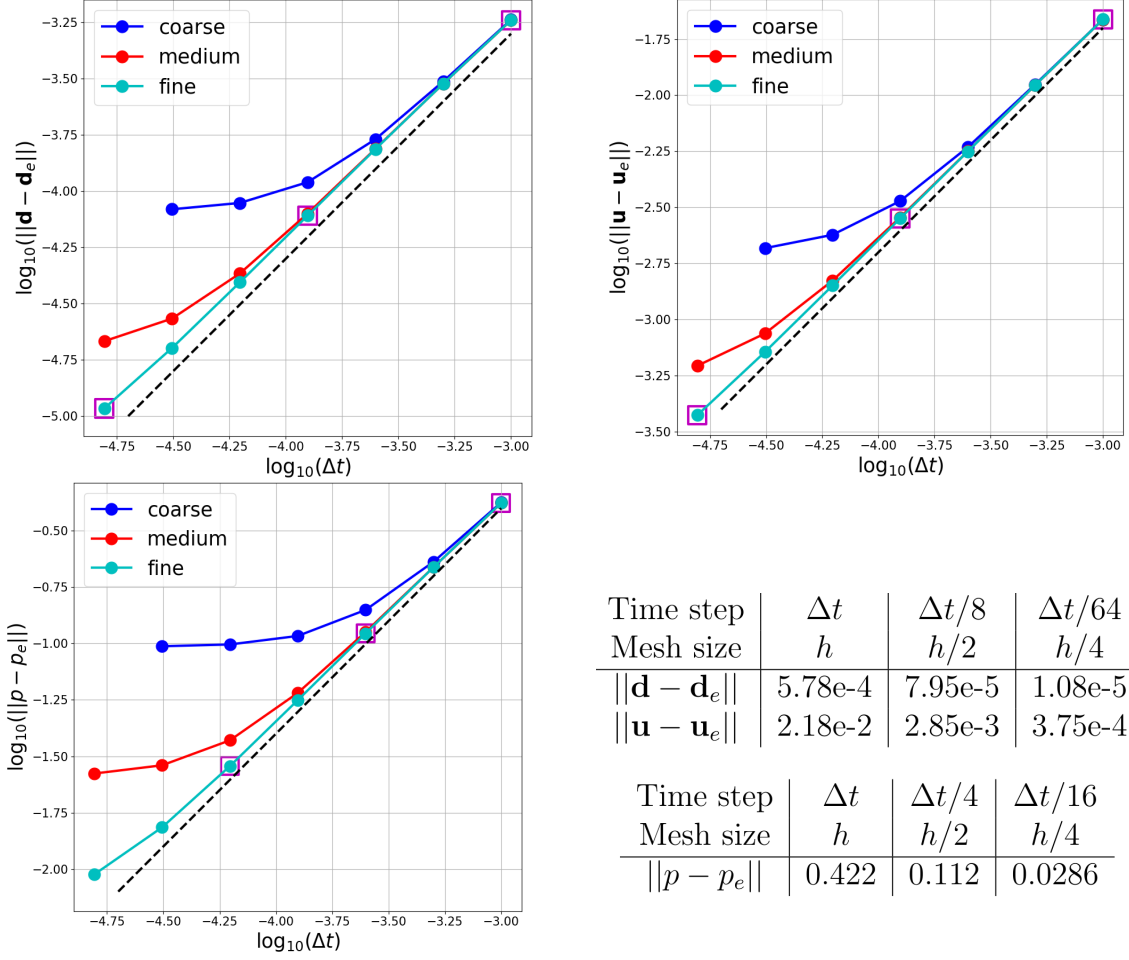


Figure 4: Spatiotemporal convergence of the displacement, velocity and pressure in space $L^2([0, T_1]; L^2(\Omega_1))$, where Ω_1 is the reference computational domain at $t = 0$. The two tables show the errors corresponding to the squared points in the graphs, which indicate the optimal convergence of backward Euler and P_2P_1 element for the time and the space discretisations respectively. The size of the coarse mesh is $h = 0.1$ and the initial time step $\Delta t = 10^{-3}$.

215 4. Problem II: compressed concentric discs

In this case, both the fluid velocity and the solid displacement only have components along the radial direction: $\mathbf{u} = u\mathbf{e}_r$ and $\mathbf{d} = d\hat{\mathbf{e}}_r$. Additionally, both $u = u(r, t)$ and $d = d(R, t) = r - R$ are independent of $\theta = \hat{\theta}$, and the pressure $p = p(r, t)$ is also independent of θ (or $\hat{\theta}$). Let $u' = \partial_r u$ and $p' = \partial_r p$ for notation convenience.

220 4.1. Fluid equations

Noticing that $\dot{\mathbf{e}}_r = \dot{\theta}\mathbf{e}_\theta = (u_\theta/r)\mathbf{e}_\theta = 0$, the inertial term can be expressed as:

$$\dot{\mathbf{u}} = \frac{d}{dt}(u_r\mathbf{e}_r) = \dot{u}\mathbf{e}_r = (\partial_t u + uu')\mathbf{e}_r. \quad (31)$$

Applying operator $\nabla \cdot \nabla$ to $\mathbf{u} = u_r \mathbf{e}_r$, we have

$$\nabla \cdot \nabla \mathbf{u} = \left(u'' + \frac{u'}{r} - \frac{u}{r^2} \right) \mathbf{e}_r. \quad (32)$$

These then yield the momentum equation

$$\rho^f (\partial_t u + uu') = \mu^f \left(u'' + \frac{u'}{r} - \frac{u}{r^2} \right) - p', \quad (33)$$

by substituting equations (31) and (32) into (1).

225 The continuity equation (2) becomes:

$$\nabla \cdot \mathbf{u} = \left(\mathbf{e}_r \partial_r + \frac{1}{r} \mathbf{e}_\theta \partial_\theta \right) \cdot (u \mathbf{e}_r) = \partial_r u + \frac{u}{r} = \frac{(ru)'}{r} = 0. \quad (34)$$

Finally, equation (34) may be substituted into equation (33) to obtain a simplified form of the momentum equation:

$$\rho^f (\partial_t u + uu') + p' = \mu^f \left(u' + \frac{u}{r} \right)' = 0. \quad (35)$$

4.2. Solid equations

Apply the operators $\hat{\nabla}$ and $\hat{\nabla} \cdot \hat{\nabla}$ to the displacement vector, and let $d' = \partial_R d$, then

$$\hat{\nabla} \mathbf{d} = \left(\hat{\mathbf{e}}_r \partial_R + \frac{1}{R} \hat{\mathbf{e}}_\theta \partial_\theta \right) (d \hat{\mathbf{e}}_r) = d' \hat{\mathbf{e}}_r \hat{\mathbf{e}}_r + \frac{d}{R} \hat{\mathbf{e}}_\theta \hat{\mathbf{e}}_\theta, \quad (36)$$

$$\hat{\nabla}^\top \mathbf{d} = d' \hat{\mathbf{e}}_r \hat{\mathbf{e}}_r + \frac{d}{R} \hat{\mathbf{e}}_\theta \hat{\mathbf{e}}_\theta = \hat{\nabla} \mathbf{d}, \quad (37)$$

$$\hat{\nabla} \cdot \hat{\nabla} \mathbf{d} = \left(d'' + \frac{d'}{R} - \frac{d}{R^2} \right) \hat{\mathbf{e}}_r. \quad (38)$$

Similar to the continuity equation of the fluid,

$$\hat{\nabla} \cdot \mathbf{d} = \left(\hat{\mathbf{e}}_r \partial_R + \frac{1}{R} \hat{\mathbf{e}}_\theta \partial_\theta \right) \cdot (d \hat{\mathbf{e}}_r) = d' + \frac{d}{R}, \quad (39)$$

which however is not zero. Instead, applying the Nabla operator (11) to $\hat{\nabla} \cdot \mathbf{d}$, we have

$$\hat{\nabla} (\hat{\nabla} \cdot \mathbf{d}) = \left(\hat{\mathbf{e}}_r \partial_R + \frac{1}{R} \hat{\mathbf{e}}_\theta \partial_\theta \right) \left(d' + \frac{d}{R} \right) = \left(d' + \frac{d}{R} \right)' \hat{\mathbf{e}}_r. \quad (40)$$

Finally, substituting equations (38) and (40) into the solid equation (3), we obtain

$$\rho^s \ddot{d} = (2\mu^s + \lambda^s) \left(d' + \frac{d}{R} \right)'. \quad (41)$$

235 *4.3. Boundary conditions*

As discussed in Section 3, the fluid equation (35) is expressed in the current or physical domain corresponding to the reference domain $[R_1, R_2]$, while the solid equation (41) is expressed directly in the reference domain $[R_0, R_1]$. We use the Lagrangian mapping to find the current domain for the fluid, i.e., extending the solid displacement $d(R, t)$ ($R \in [R_0, R_1]$) to the displacement of the fluid particles $\xi(R, t)$ ($R \in [R_1, R_2]$), with $\xi(R_1, t) = d(R_1, t)$ at the interface. Let $r_1(t) = R_1 + \xi(R_1, t)$ and $r_2(t) = R_2 + \xi(R_2, t)$, then $r(R, t) = R + \xi(R, t)$ with $R \in [R_1, R_2]$ represents a general point in the current domain $[r_1(t), r_2(t)]$.

With the above notations, the continuity of normal stress at $R = R_1$ or $r = r_1(t)$ requires that:

$$\mu^s \left(\hat{\nabla} \mathbf{d} + \hat{\nabla}^\top \mathbf{d} \right) \cdot \hat{\mathbf{e}}_r + \lambda^s \left(\hat{\nabla} \cdot \mathbf{d} \right) \mathbf{I} \cdot \hat{\mathbf{e}}_r = \mu^f \left(\nabla \mathbf{u} + \nabla^\top \mathbf{u} \right) \cdot \mathbf{e}_r - p \mathbf{I} \cdot \mathbf{e}_r, \quad (42)$$

245 or equivalently,

$$\begin{aligned} & 2\mu^s \left(d'(R_1, t) \hat{\mathbf{e}}_r \hat{\mathbf{e}}_r + \frac{d(R_1, t)}{R_1} \hat{\mathbf{e}}_\theta \hat{\mathbf{e}}_\theta \right) \cdot \hat{\mathbf{e}}_r + \lambda^s \left(d'(R_1, t) + \frac{d(R_1, t)}{R_1} \right) (\hat{\mathbf{e}}_r \hat{\mathbf{e}}_r + \hat{\mathbf{e}}_\theta \hat{\mathbf{e}}_\theta) \cdot \hat{\mathbf{e}}_r \\ & = \mu^f \left(u'(r_1, t) \mathbf{e}_r \mathbf{e}_r + \frac{u(r_1, t)}{r_1(t)} \mathbf{e}_\theta \mathbf{e}_\theta \right) \cdot \mathbf{e}_r - p(r_1, t) (\mathbf{e}_r \mathbf{e}_r + \mathbf{e}_\theta \mathbf{e}_\theta) \cdot \mathbf{e}_r. \end{aligned} \quad (43)$$

\Rightarrow

$$2\mu^s d'(R_1, t) + \lambda^s \left(d'(R_1, t) + \frac{d(R_1, t)}{R_1} \right) = \mu^f u'(r_1, t) - p(r_1, t). \quad (44)$$

Other boundary conditions include:

$$d(R_0, t) = 0 \quad (45)$$

$$\dot{d}(R_1, t) = u(r_1(t), t) \quad (46)$$

$$\mu^f u'(r_2, t) - p(r_2, t) = \bar{p}(t) \quad (47)$$

where (47) specifies the normal stress at the outer fluid boundary.

4.4. Analytical solution

250 Assuming the solution of equation (41) is periodic and separable with respect to R and t , then it can be represented by the real or imaginary part of a complex form: $d(R, t) = z(R)e^{i\omega t}$. This representation enables us to derive the equation for $d(R)$ by substituting $z(R)e^{i\omega t}$ into (41), yielding:

$$-\rho^s \omega^2 z = (2\mu^s + \lambda^s) \left(z'' + \frac{z'}{R} - \frac{z}{R^2} \right). \quad (48)$$

Let $\sqrt{\rho^s \omega^2 / (2\mu^s + \lambda^s)} = k^s$, the above equation can be rewritten as:

$$R^2 z'' + R z' + [(k^s R)^2 - 1]z = 0. \quad (49)$$

255 By change of variable: $k^s R = x$, the above equation becomes the Bessel's ODE of order one.

$$x^2 \frac{d^2 z}{dx^2} + x \frac{dz}{dx} + (x^2 - 1)z = 0, \quad (50)$$

with a general solution

$$z(R(x)) = c_1 J_1(x) + c_2 Y_1(x), \quad (51)$$

where $J_1(x)$ and $Y_1(x)$ are the first and second kind Bessel functions, respectively, of order one as follows:

$$J_1(x) = \sum_{m=0}^{\infty} \frac{(-1)^m}{m!(m+1)!} \left(\frac{x}{2}\right)^{2m+1}, \quad (52)$$

$$\frac{\pi}{2} Y_1(x) = \left(\gamma + \ln \frac{x}{2}\right) J_1(x) - \frac{1}{x} + \frac{1}{2} \sum_{m=1}^{\infty} \frac{(-1)^m (H_{m-1} + H_m)}{(m-1)!m!} \left(\frac{x}{2}\right)^{2m-1}. \quad (53)$$

with $H_0 = 0$, $H_m = 1 + 1/2 + 1/3 + \dots + 1/m$ and $\gamma = \lim_{m \rightarrow \infty} (H_m - \ln m)$. The solution of equation (49) can then be expressed as:

$$z(R) = c_1 J_1(k^s R) + c_2 Y_1(k^s R), \quad (54)$$

with the constants c_1 and c_2 being determined by the boundary conditions later. Let the $d(R, t) = z(R) \sin(\omega t)$ being the solution of (41), we derive the solution of fluid equations (34) and (35) as follows:

First, the continuity equation (34) indicates that ru is a constant: independent of r but possibly dependent of t . Recall the mapping between $r \in [r_1(t), r_2(t)]$ and $R \in [R_1, R_2]$: $r(R, t) = R + \xi(R, t)$, we have

$$ru = (R_1 + d(R_1, t)) \dot{d}(R_1, t), \quad (55)$$

due to the interface condition (46). This solves for the fluid velocity as:

$$u(r, t) = \frac{[R_1 + z(R_1) \sin(\omega t)] z(R_1) \omega \cos(\omega t)}{r}. \quad (56)$$

Notice that the initial condition of the velocity is determined the expression in (56), which cannot be zero generally, although the initial condition for the displacement is zero. The pressure can then be solved by the momentum equation (35)

$$p'(r, t) = \frac{z(R_1) \rho^f \omega^2 [R_1 \sin(\omega t) - z(R_1) \cos(2\omega t)]}{r} - \rho^f \frac{(u^2)'}{2} \quad (57)$$

Integrate to obtain the expression of $p(x, t)$:

$$p(r, t) = z(R_1) \rho^f \omega^2 [R_1 \sin(\omega t) - z(R_1) \cos(2\omega t)] \ln |r| - \rho^f \frac{u^2(r, t)}{2} + p^0(t). \quad (58)$$

The constant p^0 can be computed using the continuity of normal stress at the interface (44):

$$(2\mu^s + \lambda^s)z'(R_1) \sin(\omega t) + \lambda^s z(R_1) \sin(\omega t)/R_1 = \mu^f u'(r_1, t) - p(r_1, t), \quad (59)$$

275 \Rightarrow

$$\begin{aligned} -p^0(t) &= (2\mu^s + \lambda^s)z'(R_1) \sin(\omega t) + \lambda^s z(R_1) \sin(\omega t)/R_1 \\ &+ \frac{\mu^f z(R_1)\omega \cos(\omega t)}{r_1(t)} - \rho^f \frac{u^2(r_1(t), t)}{2} \\ &+ z(R_1)\rho^f \omega^2 [R_1 \sin(\omega t) - z(R_1) \cos(2\omega t)] \ln |r_1(t)| \end{aligned} \quad (60)$$

Substituting (60) into (58), we have

$$\begin{aligned} p(r, t) &= z(R_1)\rho^f \omega^2 [R_1 \sin(\omega t) - z(R_1) \cos(2\omega t)] \ln \left| \frac{r}{r_1(t)} \right| \\ &- \rho^f \frac{u^2(r, t) - u^2(r_1(t), t)}{2} - \frac{\mu^f z(R_1)\omega \cos(\omega t)}{r_1(t)} \\ &- (2\mu^s + \lambda^s)z'(R_1) \sin(\omega t) - \lambda^s z(R_1) \sin(\omega t)/R_1, \end{aligned} \quad (61)$$

where $r_1(t) = R_1 + z(R_1) \sin(\omega t)$.

280 Finally, the two constants c_1 and c_2 in the expression of $z(R)$ can be determined by two boundary conditions: (45) $\Rightarrow z(R_0) = 0$ and (47) $\Rightarrow p(r_2, t) = \mu^f u'(r_2, t) - \bar{p}(t)$, given $\bar{p}(t)$. However, because of the complicated form of $p(r, t)$, it is difficult to solve for $z(R_1)$ from the second condition. We simply specify $z(R_1)$ as \bar{d} – the largest displacement at R_1 , to determine the constants c_1 and c_2 first, and then write down the expression of $\bar{p}(t)$ for the problem. To express c_1 and c_2 explicitly, we have the linear system

$$z(R_0) = J_1(k^s R_0)c_1 + Y_1(k^s R_0)c_2 = 0, \quad (62)$$

$$z(R_1) = J_1(k^s R_1)c_1 + Y_1(k^s R_1)c_2 = \bar{d}, \quad (63)$$

285 whose solution can be expressed as:

$$\begin{pmatrix} c_1 \\ c_2 \end{pmatrix} = \frac{1}{\det} \begin{pmatrix} Y_1(k^s R_1) & -Y_1(k^s R_0) \\ -J_1(k^s R_1) & J_1(k^s R_0) \end{pmatrix} \begin{pmatrix} 0 \\ \bar{d} \end{pmatrix}, \quad (64)$$

where $\det = J_1(k^s R_0)Y_1(k^s R_1) - J_1(k^s R_1)Y_1(k^s R_0)$.

290 **Remark 5.** *To accurately evaluate Bessel functions is not trivial, especially for large arguments. Classically, power series are used for small arguments and asymptotic series for large arguments. Nonlinear sequence transformations are employed for intermediate arguments to bridge the gap between the asymptotic expansion for large arguments and the Taylor expansion for small arguments [69, 70]. Additionally, methods such as integral representation with the trapezoidal rule are adopted to compute Bessel functions [71–73]. Our implementation in this article is based on the scipy.special library [74].*

4.5. Mapping between r and R

295 Since the solutions of fluid and solid are expressed in different configurations. In order to display and visualise results, such as showing the velocity of both the fluid and solid across $[R_0, R_2]$, it is necessary to write down the mapping between r and R explicitly. For $R \in [R_0, R_1]$, $r = R + z(R) \sin(\omega t)$; for $R \in [R_1, R_2]$, the mapping can be computed by solving equation (55):

$$ru = \frac{d}{dt} \left(\frac{r^2(R, t)}{2} \right) = (R_1 + z(R_1) \sin(\omega t)) z(R_1) \omega \cos(\omega t) \quad (65)$$

300 \Rightarrow

$$\frac{r^2(R, t)}{2} = R_1 z(R_1) \sin(\omega t) + \int z^2(R_1) \frac{\omega \sin(2\omega t)}{2} dt \quad (66)$$

\Rightarrow

$$\frac{r^2(R, t)}{2} = R_1 z(R_1) \sin(\omega t) - z^2(R_1) \frac{\cos(2\omega t)}{4} + C(R). \quad (67)$$

Since $r(R, 0) = R \Rightarrow C(R) = R^2/2 + z^2(R_1)/4$, therefore,

$$\frac{r^2(R, t)}{2} = R_1 z(R_1) \sin(\omega t) + z^2(R_1) \frac{\sin^2(\omega t)}{2} + \frac{R^2}{2}. \quad (68)$$

\Rightarrow

$$r^2(R, t) = R^2 + (R_1 + z(R_1) \sin(\omega t))^2 - R_1^2, \quad (69)$$

which is the relation between r and R .

305 **Remark 6.** Equation (41) possesses another form of solution: $d(R, t) = z(R)t$, where $z(R) = C_1 R + R/C_2$ represents the steady-state solution for (41) – an Euler PDE, with C_1 and C_2 being two constants. Consequently, this would yield an alternative solution for the FSI problem, albeit with distinct boundary conditions.

4.6. Numerical validation

310 We validate the analytical solutions of the solid displacement $d(R, t) = z(R) \sin(\omega t)$ as well as its velocity $u(R, t) = z(R) \omega \cos(\omega t)$, together with the fluid velocity (56) and pressure (61), against the results of two-dimensional numerical simulations. We compare all the quantities in the reference configuration based on the mapping as described in Section 4.5: the results for a typical parameter set shown in Table 2. We set $z(R_1) = \bar{d} = 0.05$ to compute the coefficients c_1 and c_2 in (63), which is $\bar{d}/(R_1 - R_0) = 5\%$ of deformation of the width of the solid domain.

ρ^f	ρ^s	μ^f	μ^s	λ^s	R_0	R_1	R_2	ω
1	2	2	10	100	3	4	5	2π

Table 2: A group of parameters for the compressed disc.

It can be seen in Figure 6 how the simulation results, based on a relatively coarse mesh (see Figure 5), converge to the analytical solution over time. The evolution of the fluid-solid interface is plotted in Figure 7, from which it can be observed that the error gradually increases as time progresses. The results of spatiotemporal convergence are displayed in Figure 8, with the last figure (bottom-right) showing the time convergence of the $L^2(\Omega_2)$ error at $T_2 = 0.5$ on the medium mesh. We find that the time convergence rate is not optimal; this is because there is an accumulated error when comparing the last figure (bottom-right) in Figure 8 to the other three. The accumulated error may be due to our implementation of the Bessel functions and the data transfer between Python and FreeFem++, which needs further investigations. The lack of optimal mesh convergence is understandable because FreeFem++ does not use isoparametric mesh for P_2P_1 elements. Our focus here is on validating the analytical solution, leaving the testing of the convergence rate of the numerical scheme for future study.

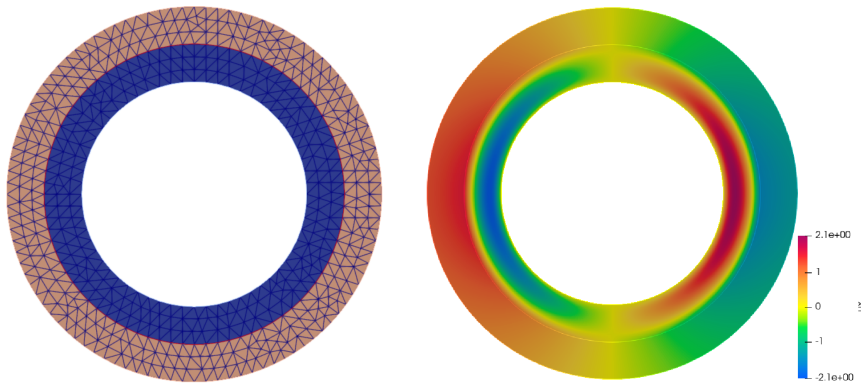


Figure 5: A coarse mesh with 572 nodes and 1225 triangle (left), and the horizontal velocity profile at $t = 0.5$ (right).

Remark 7. *This problem can pose significant challenges for numerical simulations when moving the mesh, particularly when multiple compression waves propagate within the solid. For instance, setting $R_0 = 1$ in the parameter set outlined in Table 2 and $\bar{d} = 0.15$ (equivalent to 5% of the width of the solid domain $R_1 - R_0$ results in the emergence of a rapidly propagating wave within the solid, as illustrated in Figure B.12.*

5. Problem III: rotating concentric discs

We assume pure rotation for this problem. For the fluid, the velocity vector $\mathbf{u} = u\mathbf{e}_\theta$ only has the tangential component $u = u(r, t)$, which is independent of θ . The pressure $p = p(r, t)$ is also independent of θ . For the solid, pure rotation means $r = R$ is independent of time in the position vector $r\mathbf{e}_r$, so its velocity, $\frac{d}{dt}(r\mathbf{e}_r) = r\dot{\theta}\mathbf{e}_\theta$, only has the tangential component. Assuming the angular displacement $\alpha = \theta - \hat{\theta} = \alpha(r, t)$ is independent of $\hat{\theta}$, then $\theta = \alpha + \hat{\theta}$, $\partial_r\theta = \partial_r\alpha$, and $\partial_{\hat{\theta}}\theta = 1$, which will be used in the following derivations. Finally, let $\dot{u} = \frac{du}{dt}$, $\dot{\alpha} = \frac{d\alpha}{dt}$, $u' = \partial_r u$, and $\alpha' = \partial_r \alpha$ for the convenience of notation.

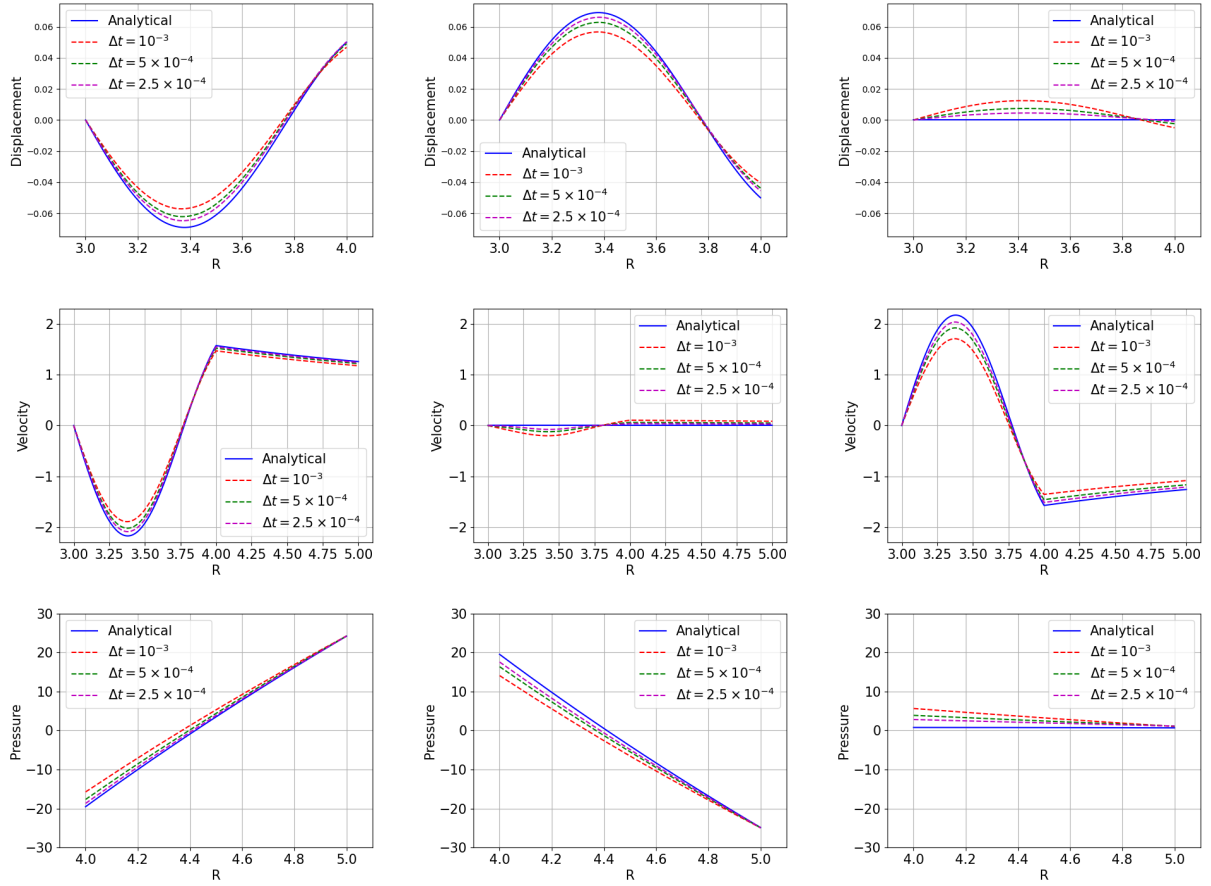


Figure 6: Comparison of displacement (first row), velocity (second row), pressure (third row) at three at $t = 0.25$, $t = 0.35$ and $t = 0.5$ from left to right, except the plot of velocity at the second row and first column which is at $t = 0.2$, because the velocity profile at $t = 0.25$ is very similar to $t = 0.35$.

5.1. Fluid equations

Since $\dot{\mathbf{e}}_\theta = -\dot{\theta}\mathbf{e}_r = -(u/r)\mathbf{e}_r$, the inertial term can be expressed as:

$$\dot{\mathbf{u}} = \dot{u}\mathbf{e}_\theta - (u^2/r)\mathbf{e}_r. \quad (70)$$

345

Apply the Nabla operator to $\mathbf{u} = u\mathbf{e}_\theta$:

$$\nabla \mathbf{u} = \left(\mathbf{e}_r \partial_r + \mathbf{e}_\theta \frac{1}{r} \partial_\theta \right) (u\mathbf{e}_\theta) = \partial_r u \mathbf{e}_r \mathbf{e}_\theta - \frac{1}{r} u \mathbf{e}_\theta \mathbf{e}_r, \quad (71)$$

$$\nabla \cdot \nabla \mathbf{u} = \left(\partial_{rr} + \frac{1}{r} \partial_r + \frac{1}{r^2} \partial_{\theta\theta} \right) (u\mathbf{e}_\theta) = \left(\partial_{rr} u + \frac{1}{r} \partial_r u_\theta - \frac{u}{r^2} \right) \mathbf{e}_\theta. \quad (72)$$

$$\nabla p^f = \left(\mathbf{e}_r \partial_r + \mathbf{e}_\theta \frac{1}{r} \partial_\theta \right) p = \partial_r p^f \mathbf{e}_r. \quad (73)$$

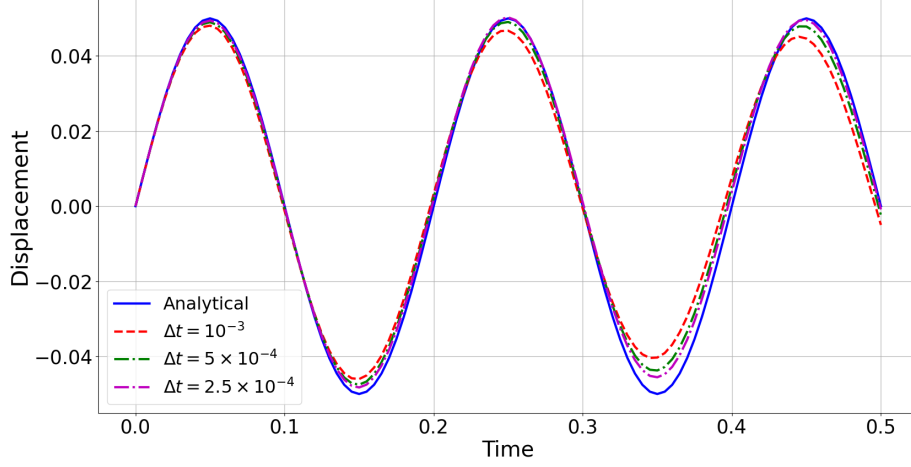


Figure 7: Displacement of the interface as a function of time.

The continuity equation (2) is automatically satisfied since

$$\nabla \cdot \mathbf{u} = \left(\mathbf{e}_r \partial_r + \frac{1}{r} \mathbf{e}_\theta \partial_\theta \right) \cdot (u \mathbf{e}_\theta) = 0. \quad (74)$$

Combining the above equations(70), 72) and (73), the momentum equation (1) can be expressed, in the polar coordinate system, as:

$$\rho^f \dot{u} = \mu^f (u'' + u'/r - u/r^2), \quad (75)$$

and

$$-\rho^f u^2/r = -\partial_r p^f. \quad (76)$$

5.2. Solid equations

We use a large displacement formulation of an incompressible Neo-Hookean solid model. We apply the Nabla operator $\hat{\nabla}$ to the position vector $r \mathbf{e}_r$ to compute the deformation tensor:

$$\mathbf{F} = \hat{\nabla}(r \mathbf{e}_r) = \left(\hat{\mathbf{e}}_r \partial_R + \frac{1}{R} \hat{\mathbf{e}}_\theta \partial_{\hat{\theta}} \right) (r \mathbf{e}_r) = \hat{\mathbf{e}}_r \mathbf{e}_r + \hat{\mathbf{e}}_r \mathbf{e}_\theta (r\theta') + \hat{\mathbf{e}}_\theta \mathbf{e}_\theta, \quad (77)$$

due to $\partial_R \mathbf{e}_r = \mathbf{e}_\theta \partial_R \theta = \mathbf{e}_\theta \theta'$ and $\partial_{\hat{\theta}} \mathbf{e}_r = \mathbf{e}_\theta \partial_{\hat{\theta}} \theta = \mathbf{e}_\theta$. Then,

$$\begin{aligned} \mathbf{F} \mathbf{F}^\top &= (\hat{\mathbf{e}}_r \mathbf{e}_r + \hat{\mathbf{e}}_r \mathbf{e}_\theta (r\theta') + \hat{\mathbf{e}}_\theta \mathbf{e}_\theta) \cdot (\mathbf{e}_r \hat{\mathbf{e}}_r + \mathbf{e}_\theta \hat{\mathbf{e}}_r (r\theta') + \mathbf{e}_\theta \hat{\mathbf{e}}_\theta) \\ &= [1 + (r\theta')^2] \hat{\mathbf{e}}_r \hat{\mathbf{e}}_r + (r\theta') \hat{\mathbf{e}}_r \hat{\mathbf{e}}_\theta + (r\theta') \hat{\mathbf{e}}_\theta \hat{\mathbf{e}}_r + \hat{\mathbf{e}}_\theta \hat{\mathbf{e}}_\theta, \end{aligned} \quad (78)$$

and further

$$\mathbf{F} \mathbf{F}^\top - \mathbf{I} = (r\theta')^2 \hat{\mathbf{e}}_r \hat{\mathbf{e}}_r + (r\theta') \hat{\mathbf{e}}_r \hat{\mathbf{e}}_\theta + (r\theta') \hat{\mathbf{e}}_\theta \hat{\mathbf{e}}_r. \quad (79)$$

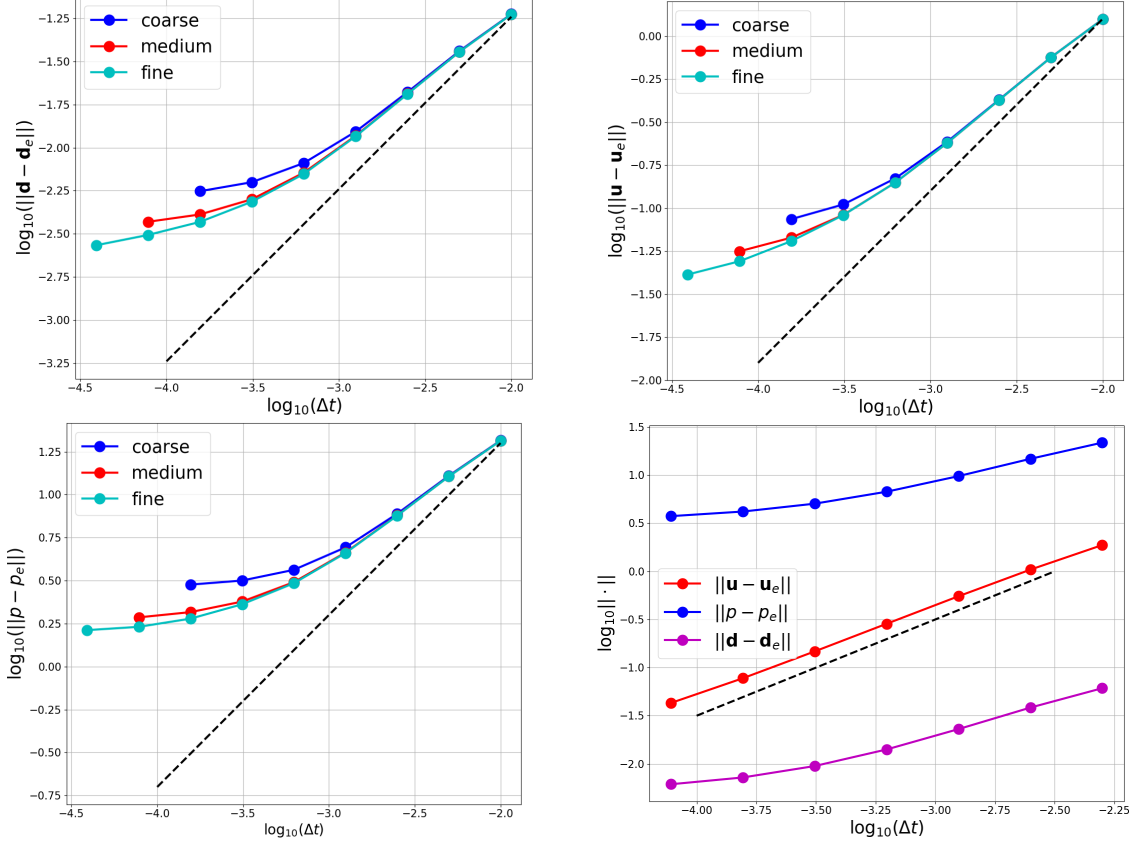


Figure 8: From left to right and top to bottom, the first three plots are spatiotemporal convergence of the displacement, velocity and pressure in space $L^2([0, T_2]; L^2(\Omega_2))$, where $T_2 = 0.5$, and Ω_2 is the reference computational domain at $t = 0$. The last plot is the time convergence of the $L^2(\Omega_2)$ error of the velocity, displacement and pressure at $T_2 = 0.5$ on the medium mesh. The mesh size is defined by the maximum size of the elements.

In the spirit of expressing the solid equation in the current configuration, we replace $(\hat{\mathbf{e}}_r, \hat{\mathbf{e}}_\theta)$ by $(\mathbf{e}_r, \mathbf{e}_\theta)$ in equation (79) using the relation (12):

$$\mathbf{F}\mathbf{F}^\top - \mathbf{I} = \tau_{11}\mathbf{e}_r\mathbf{e}_r + \tau_{22}\mathbf{e}_\theta\mathbf{e}_\theta + \tau_{12}\mathbf{e}_\theta\mathbf{e}_r + \tau_{21}\mathbf{e}_r\mathbf{e}_\theta, \quad (80)$$

with $\tau_{11} = (r\alpha')^2 \cos^2 \alpha + (r\alpha') \sin(2\alpha)$, $\tau_{22} = (r\alpha')^2 \sin^2 \alpha - (r\alpha') \sin(2\alpha)$ and $\tau_{12} = \tau_{21} =$
 360 $(r\alpha') \cos(2\alpha) - \frac{(r\alpha')^2}{2} \sin(2\alpha)$, noticing that $\theta' = \alpha'$. We then have

$$\nabla \cdot (\mathbf{F}\mathbf{F}^\top - \mathbf{I}) = \partial_r \tau_{12} \mathbf{e}_\theta + \frac{2\tau_{12}}{r} \mathbf{e}_\theta + \partial_r \tau_{11} \mathbf{e}_r + \frac{\tau_{11} - \tau_{22}}{r} \mathbf{e}_r. \quad (81)$$

The inertial term is

$$\ddot{\mathbf{d}} = \frac{d^2}{dt^2}(r\mathbf{e}_r) = \frac{d}{dt}(r\dot{\alpha}\mathbf{e}_\theta) = r\ddot{\alpha}\mathbf{e}_\theta - r\dot{\alpha}^2\mathbf{e}_r, \quad (82)$$

bearing in mind that $\dot{\theta} = \dot{\alpha}$.

Substituting equations (81) and (82) into the solid equation (4), we have

$$\rho^s r \ddot{\alpha} = \mu^s [\partial_r \tau_{12} + 2\tau_{12}/r], \quad (83)$$

and

$$-\rho^s r \dot{\alpha}^2 = \mu^s [\partial_r \tau_{11} + (\tau_{11} - \tau_{22})/r] - \partial_r p^s. \quad (84)$$

365 5.3. Boundary and initial conditions

The continuity of normal stress at the interface $r = R_1$ indicates that:

$$\mu^s (\mathbf{F}\mathbf{F}^\top - \mathbf{I}) \cdot \mathbf{e}_r - p^s \mathbf{I} \cdot \mathbf{e}_r = \mu^f (\nabla^\top \mathbf{u} + \nabla \mathbf{u}) \cdot \mathbf{e}_r - p^f \mathbf{I} \cdot \mathbf{e}_r, \quad (85)$$

\Rightarrow

$$\mu^s (\tau_{11} \mathbf{e}_r + \tau_{12} \mathbf{e}_\theta) - p^s \mathbf{e}_r = \mu^f \left(u' - \frac{u}{r} \right) \mathbf{e}_\theta - p^f \mathbf{e}_r \quad \text{at } r = R_1. \quad (86)$$

\Rightarrow

$$\mu^s \tau_{12}(\alpha(R_1, t)) = \mu^f [u'(R_1, t) - u(R_1, t)/R_1] \quad (87)$$

$$\mu^s \tau_{11}(\alpha(R_1, t)) = p^s(R_1, t) - p^f(R_1, t) \quad (88)$$

370 Other boundary conditions include:

$$\alpha(R_0, t) = 0, \quad (89)$$

$$R_1 \dot{\alpha}(R_1, t) = u(R_1, t), \quad (90)$$

$$u(R_2, t) = \bar{u}(t). \quad (91)$$

Initial conditions are:

$$\alpha(r, 0) = \alpha_0 \quad \text{in } [R_0, R_1], \quad (92)$$

$$u(r, 0) = u_0 \quad \text{in } [R_1, R_2]. \quad (93)$$

375 5.4. A one-velocity monolithic method

In this section, we use a finite element method to solve the velocity equation (75) of the fluid and the angular displacement equation (83) of the solid together in a fully-coupled manner. In addition, we express the angular displacement α in terms of velocity and only solve for one velocity field in domain $[R_0, R_2]$. For this method, the continuity of the velocity at the interface (90) is automatically satisfied. The pressure equations (76) and (84) are decoupled from the momentum equations, and will be solved as a postprocess.

Given a test function $v(r) \in H_0^1[R_0, R_2] = \{v : v \in H^1[R_0, R_2], v(R_0, t) = 0\}$, the weak form of (83) can be expressed as:

$$\rho^s \int_{R_0}^{R_1} r \ddot{\alpha} v dr = \mu^s \int_{R_0}^{R_1} \tau_{12}(\alpha) [2v/r - v'] dr + \mu^s \tau_{12}(\alpha(R_1, t)) v(R_1). \quad (94)$$

Considering the interface condition (87), the weak form of (75) may be expressed as:

$$\begin{aligned} \rho^f \int_{R_1}^{R_2} \dot{u}v &= \mu^f \int_{R_1}^{R_2} [(u' - u/r)' + 2(u'/r - u/r^2)]vdr \\ &= -\mu^f [u'(R_1, t) - u(R_1, t)/R_1] + \mu^f \int_{R_1}^{R_2} (u' - u/r)(2v/r - v')dr. \end{aligned} \quad (95)$$

385 The sum of equations (94) and (95) leads to the monolithic formulation as follows:
 Given the initial values α_0 in (92) and u_0 in (93), find $u(r, t) \in H^1[R_0, R_2]$ such that $\forall v(r) \in H_0^1[R_0, R_2]$, the following equation holds:

$$\rho \int_{R_0}^{R_2} \dot{u}vdr = \mu^s \int_{R_0}^{R_1} \tau_{12}(\alpha)[2v/r - v']dr + \mu^f \int_{R_1}^{R_2} (u' - u/r)(2v/r - v')dr, \quad (96)$$

where $\rho = \rho^s 1_{[R_0, R_1]} + \rho^f 1_{[R_1, R_2]}$ and $r\dot{\alpha} = u$ in $[R_0, R_1]$.

390 Function $\tau_{12}(\alpha)$ in (96) is non-linear in terms of α , we use the Newton method to linearise it as follows:

$$\tau_{12}(\alpha) \approx \tau_{12}(\alpha^k) + \delta\tau_{12}(\alpha^k; \alpha - \alpha^k), \quad (97)$$

where α^k is a reference point and $\delta\tau_{12}(\alpha; \beta)$ is the first order Gateaux variation at α along direction β [2, 75]:

$$\delta\tau_{12}(\alpha; \beta) = \left. \frac{d}{d\epsilon} \tau_{12}(\alpha + \epsilon\beta) \right|_{\epsilon=0}. \quad (98)$$

With this definition, we compute the variations of $\tau_{12}(\alpha)$:

$$\delta\tau_{12}(\alpha; \delta\alpha) = r\delta\alpha' \cos(2\alpha) - 2r\alpha' \sin(2\alpha)\delta\alpha - r^2\alpha' \sin(2\alpha)\delta\alpha' - (r\alpha')^2 \cos(2\alpha)\delta\alpha, \quad (99)$$

Substituting (99) into (97), with $\delta\alpha = \alpha - \alpha^k$, we have

$$\begin{aligned} \tau_{12}(\alpha) &\approx r\alpha' \cos(2\alpha^k) - 2r(\alpha^k)' \sin(2\alpha^k)(\alpha - \alpha^k) - r^2(\alpha^k)' \sin(2\alpha^k)(\alpha - \alpha^k)' \\ &\quad - [r(\alpha^k)']^2 \cos(2\alpha^k)(\alpha - \alpha^k) - \frac{(r(\alpha^k)')^2}{2} \sin(2\alpha^k). \end{aligned} \quad (100)$$

395 Finally, we consider a linearisation in time. Given the previous values α_n and u_n at time t_n where $n = 0, 1, 2, \dots$, we use a uniform time step Δt to compute α_{n+1} and u_{n+1} . Since $r\dot{\alpha} = u$, we express $\alpha_{n+1} = \alpha_n + u_{n+1}\Delta t/r$ based on the backward Euler scheme. Dropping of the subscript $n + 1$ for convenience, and substituting $\alpha = \alpha_n + u\Delta t/r$ and $\alpha' = \alpha'_n + \Delta t(u'/r - u/r^2)$, together with (100), to equation (96), we have the linearised
 400 one-velocity monolithic formulation after time discretisation:

Given α_n and u_n at time t_n , find $u_{n+1} = u(r, t) \in H^1[R_0, R_2]$ such that $\forall v(r) \in H_0^1[R_0, R_2]$, the following equation holds:

$$\begin{aligned}
& \rho \int_{R_0}^{R_2} \frac{u - u_n}{\Delta t} v dr + \mu^f \int_{R_1}^{R_2} (u' - u/r)(v' - 2v/r) dr \\
& + \mu^s \int_{R_0}^{R_1} \Delta t [\cos(2\alpha^k) - r(\alpha^k)' \sin(2\alpha^k)] (u' - u/r)(v' - 2v/r) dr \\
& - \mu^s \int_{R_0}^{R_1} \Delta t [r((\alpha^k)')^2 \cos(2\alpha^k) + 2(\alpha^k)' \sin(2\alpha^k)] u(v' - 2v/r) dr \\
& = \mu^s \int_{R_0}^{R_1} [-r\alpha_n' \cos(2\alpha^k) + 2r(\alpha^k)' \sin(2\alpha^k) (\alpha_n - \alpha^k)] (v' - 2v/r) dr \\
& + \mu^s \int_{R_0}^{R_1} [r^2(\alpha^k)' \sin(2\alpha^k) (\alpha_n - \alpha^k)' + (r(\alpha^k)')^2 \cos(2\alpha^k) (\alpha_n - \alpha^k)] (v' - 2v/r) dr \\
& + \mu^s \int_{R_0}^{R_1} \frac{(r(\alpha^k)')^2}{2} \sin(2\alpha^k)(v' - 2v/r) dr.
\end{aligned} \tag{101}$$

The pressure is computed as a post-process. Integration of equation (84) from R_0 to $R \in (R_0, R_1]$ yields the expression of the pressure of solid:

$$p^s(R, t) = \mu^s [\tau_{11}(\alpha(R)) - \tau_{11}(\alpha(R_0))] + \mu^s \int_{R_0}^R \frac{\tau_{11} - \tau_{22}}{r} dr + \rho^s \int_{R_0}^R \frac{u^2}{r} dr, \tag{102}$$

405 given a reference pressure $p^s(R_0, t) = 0$. Integration of equation (76) from R_1 to $R \in (R_1, R_2]$ yields the expression of the fluid pressure as follows:

$$p^f(R, t) = \rho^f \int_{R_1}^R \frac{u^2}{r} dr + p^f(R_1, t), \tag{103}$$

where $p^f(R_1, t) = p^s(R_1, t) - \mu^s \tau_{11}(\alpha(R_1))$ is known from the jump condition (88).

5.5. Numerical Validation

410 It is efficient to solve the one-dimensional problem (101) to very high accuracy, a solution we refer to as the semi-analytical solution. We tested a range of parameters and compared these semi-analytical solutions to those obtained from two-dimensional simulations using the numerical method described in Appendix A. We found that the one-dimensional and two-dimensional solutions agree very well. We report the results of the parameter set in Table 3, where a periodic angular velocity profile is prescribed at boundary R_2 : $\Omega(t) = \bar{\Omega} \sin(\omega t)$ 415 with $\bar{\Omega} = 3$. Consequently, a complicated wave-like solution is created, and we have to use of a relatively fine mesh to capture this feature. A finite element mesh and the magnitude of the velocity at $t = 1$ are displayed in Figure 9 to visualise the wave pattern.

The comparison of displacement, velocity, and pressure between the 1D and 2D simulations is depicted in Figure 10. It can be observed that the results for displacement and

ρ^f	ρ^s	μ^f	μ^s	R_0	R_1	R_2	ω
1	2	2	10	3	4	5	10π

Table 3: A group of parameters for the rotating disc.

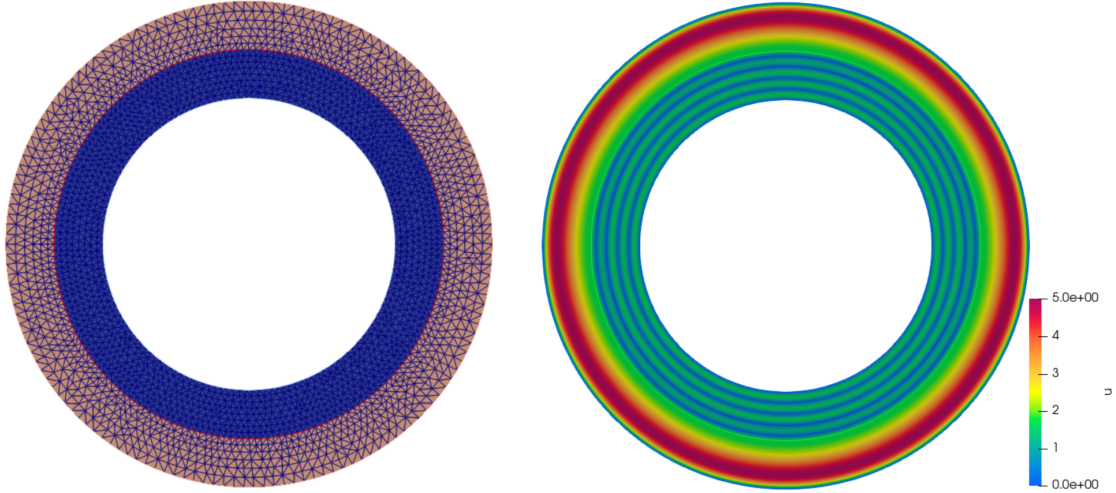


Figure 9: A coarse mesh with 2621 nodes and 5443 triangle and the magnitude of velocity profile at $t = 0.5$.

420 velocity show good agreement between the 1D and 2D simulations, while there is a noticeable discrepancy in pressure. We attribute this inconsistency in pressure to the discontinuity at $R = R_1$, despite employing the $P_2(P_1 + P_0)$ element [76], as can be seen in the last two plots of Figure 10. Consequently, there is a pressure shift within the fluid region, which in turn affects the accuracy of solid pressure as well.

425 6. Conclusion

In this paper, we propose three fluid-structure interaction problems and derive their analytical or semi-analytical solutions, which have been validated through numerical experiments. These FSI solutions fill the gap in the analytical solutions within the FSI community and contribute to the field by benchmarking numerical methods for FSI problems.

430 We also developed the one-velocity monolithic method to solve a one-dimensional non-linear problem (96) and an linear elastic problem in the reference domain (A.2). The one-velocity monolithic method is tested against the analytical solution, with results showing good agreement between them.

435 The results between the analytical and numerical solutions for the rotating disc (Problem III) do not align well for the pressure, although they match closely for the pressure and displacement. We attribute this discrepancy to the pressure discontinuity across the fluid-solid interface not being accurately captured in the numerical methods. Different numerical strategies, such as discontinuous finite elements or regularisation methods, may be explored in the future.

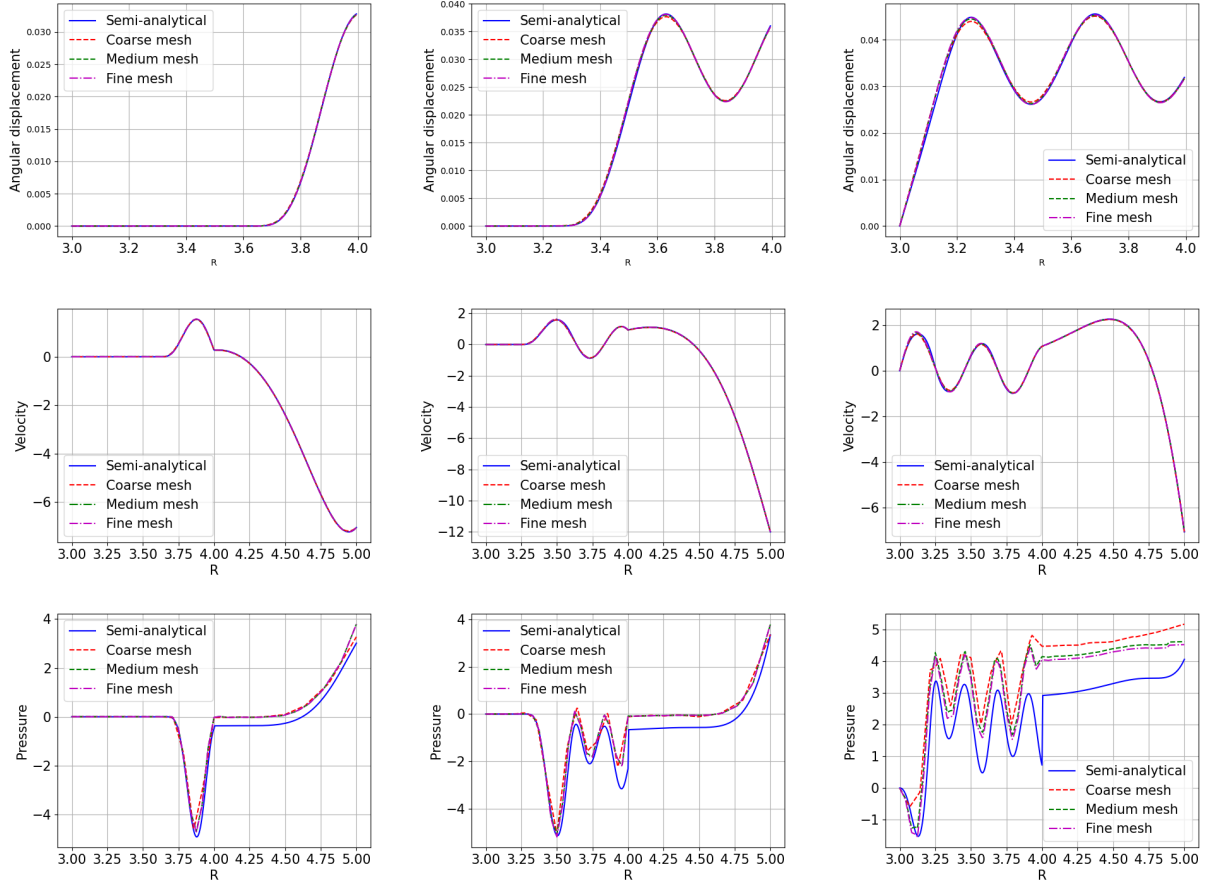


Figure 10: Comparison of angular displacement (first row), velocity (second row), and pressure (third row) at three time instances, $t = 0.2$, $t = 0.35$, and $t = 0.5$, from left to right. It is noteworthy that a maximum angular displacement of 0.045 corresponds to a maximum radial displacement of $0.045R_1 = 0.135$, which represents a 13.5% deformation of the width of the solid domain, $R_1 - R_0 = 1$.

440 Appendix A. The one-velocity numerical methods for FSI problems

In this section, we briefly introduce the numerical method used to simulate two-dimensional problems. We employ the monolithic Eulerian method, as discussed in several references [57–59], to solve for a single velocity variable across the entire fluid-structure domain $\Omega_t^f \cup \Omega_t^s$. Additionally, we utilise the arbitrary Lagrangian Eulerian method to handle the moving mesh.

Given the Cauchy stress tensor $\boldsymbol{\sigma}$ in the current configuration, the general weak form of this monolithic approach can be expressed as follows [59]:

$$\int_{\Omega} \rho (\partial_t \mathbf{u} + (\mathbf{u} - \mathbf{w}) \nabla \cdot \mathbf{u}) \delta \mathbf{u} + \int_{\Omega} \boldsymbol{\sigma} : \nabla \delta \mathbf{u} = \int_{\partial \Omega} (\boldsymbol{\sigma} \cdot \mathbf{n}) \cdot \delta \mathbf{u}, \quad (\text{A.1})$$

where $\rho = \rho^f 1_{\Omega^f} + \rho^s 1_{\Omega^s}$, $\boldsymbol{\sigma} = \boldsymbol{\sigma}^f 1_{\Omega^f} + \boldsymbol{\sigma}^s 1_{\Omega^s}$, \mathbf{w} is the prescribed mesh velocity, which may be simply obtained by solving a static linear elastic equation, \mathbf{n} is the outer normal of domain Ω .

The one-velocity method aims to express the displacement $\mathbf{d}_{n+1} = \mathbf{d}_n + \Delta t \mathbf{u}_{n+1}$ after time discretisation, solving solely for the velocity \mathbf{u}_{n+1} at time t_{n+1} for the whole FSI problem, given \mathbf{u}_n and \mathbf{d}_n at time t_n . The primary objective is then to express $\int_{\Omega} \boldsymbol{\sigma} : \nabla \delta \mathbf{u} = \int_{\Omega_t^f} \boldsymbol{\sigma}^f : \nabla \delta \mathbf{u} + \int_{\Omega_t^s} \boldsymbol{\sigma}^s : \nabla \delta \mathbf{u}$ in terms of displacement \mathbf{d} , which is discussed in the following.

455 The fluid integration expressions are the same for Problems I, II, and III: $\mathbf{d}_{n+1} = \mathbf{d}_n + \Delta t \mathbf{u}_{n+1}$ after time discretisation, and only solve for velocity \mathbf{u}_{n+1} at time t_{n+1} for the whole FSI problem, given \mathbf{u}_n and \mathbf{d}_n at time t_n . Then the main task is to express $\int_{\Omega} \boldsymbol{\sigma} : \nabla \delta \mathbf{u} = \int_{\Omega_t^f} \boldsymbol{\sigma}^f : \nabla \delta \mathbf{u} + \int_{\Omega_t^s} \boldsymbol{\sigma}^s : \nabla \delta \mathbf{u}$ in terms of displacement \mathbf{d} .

The fluid integration expressions are the same for Problems I, II, and III:

$$\int_{\Omega_t^f} \boldsymbol{\sigma}^f : \nabla \delta \mathbf{u} = \frac{\mu^f}{2} \int_{\Omega_t^f} (\nabla^\top \mathbf{u} + \nabla \mathbf{u}) : (\nabla^\top \delta \mathbf{u} + \nabla \delta \mathbf{u}) - \int_{\Omega_t^f} p \nabla \cdot \delta \mathbf{u}, \quad (\text{A.2})$$

460 but they differ in the boundary integration expression concerning the Neumann boundary condition: $\boldsymbol{\sigma} \cdot \mathbf{n} = \bar{p}(t) \mathbf{n}$ at boundary R_2 for Problem I and II, while $\boldsymbol{\sigma} \cdot \mathbf{n} = 0$ for Problem III. They also vary in the solid stress tensor $\boldsymbol{\sigma}^s$ as described through the momentum equations (3) and (4).

For Problems I and II, the first Piola-Kirchhoff stress tensor $\mathbf{P} = \mu^s (\hat{\nabla}^\top \mathbf{d} + \hat{\nabla} \mathbf{d}) + \lambda^s (\hat{\nabla} \cdot \mathbf{d}) \mathbf{I}$ is used in the reference configuration, as seen in (3). To implement the monolithic Eulerian formulation, we convert \mathbf{P} to the Cauchy stress tensor and integrate as follows:

$$\begin{aligned} \int_{\Omega_t^s} \boldsymbol{\sigma}^s : \nabla \delta \mathbf{u} &= \int_{\Omega_t^s} J^{-1} \mathbf{P} \mathbf{F}^\top : \nabla \delta \mathbf{u} \\ &= \mu^s \int_{\Omega_t^s} J^{-1} (\mathbf{F}^\top \nabla^\top \mathbf{d} + \nabla \mathbf{d} \mathbf{F}) \mathbf{F}^\top : \nabla \delta \mathbf{u} + \lambda^s \int_{\Omega_t^s} J^{-1} \text{trace}(\nabla \mathbf{d} \mathbf{F}) \text{trace}(\nabla \delta \mathbf{u} \mathbf{F}), \end{aligned} \quad (\text{A.3})$$

where $\mathbf{F} = \hat{\nabla} \mathbf{d} + \mathbf{I} = \nabla \mathbf{d} \mathbf{F} + \mathbf{I} \Rightarrow \mathbf{F} = (\mathbf{I} - \nabla \mathbf{d})^{-1}$ is computed in the current configuration. As \mathbf{F} depends on the unknown variable, a fixed-point iteration is employed to iteratively compute \mathbf{F} .

470 For Problem III, the Cauchy stress tensor $\boldsymbol{\sigma}^s = \mu^s (\mathbf{F} \mathbf{F}^\top - \mathbf{I}) - p^s \mathbf{I}$ is used as seen in (4), which can be rewritten as [59]:

$$\boldsymbol{\sigma}^s = \mu^s (\nabla^\top \mathbf{d} + \nabla \mathbf{d} - \nabla^\top \mathbf{d} \nabla \mathbf{d}) - (p^s + \mu^s (\text{trace}(\mathbf{F} \mathbf{F}^\top) - 2)) \mathbf{I}. \quad (\text{A.4})$$

For the numerical implementation of (A.4), we introduce a new variable $q^s = p^s + \mu^s (\text{trace}(\mathbf{F} \mathbf{F}^\top) - 2)$. Equation (A.4) is then expressed in terms of the displacement \mathbf{d} and the new pressure q^s .

Appendix B. Additional test cases

In this appendix, we provide a brief report on the results of some additional, yet special, test cases as supplementary material to the main content of this article. Readers may also refer to additional supporting animations at <https://yongxingwang.github.io/simulation/>.

480 *Appendix B.1. Problem I: compressed plates*

Figure B.11 shows the velocity profile, where the fluid velocity remains zero while there is a moving wave in the solid. This result is obtained by modifying the parameter set in Table 1 with $\phi = 3\pi$, in which case nothing happens in the fluid as commented in Remark 4.

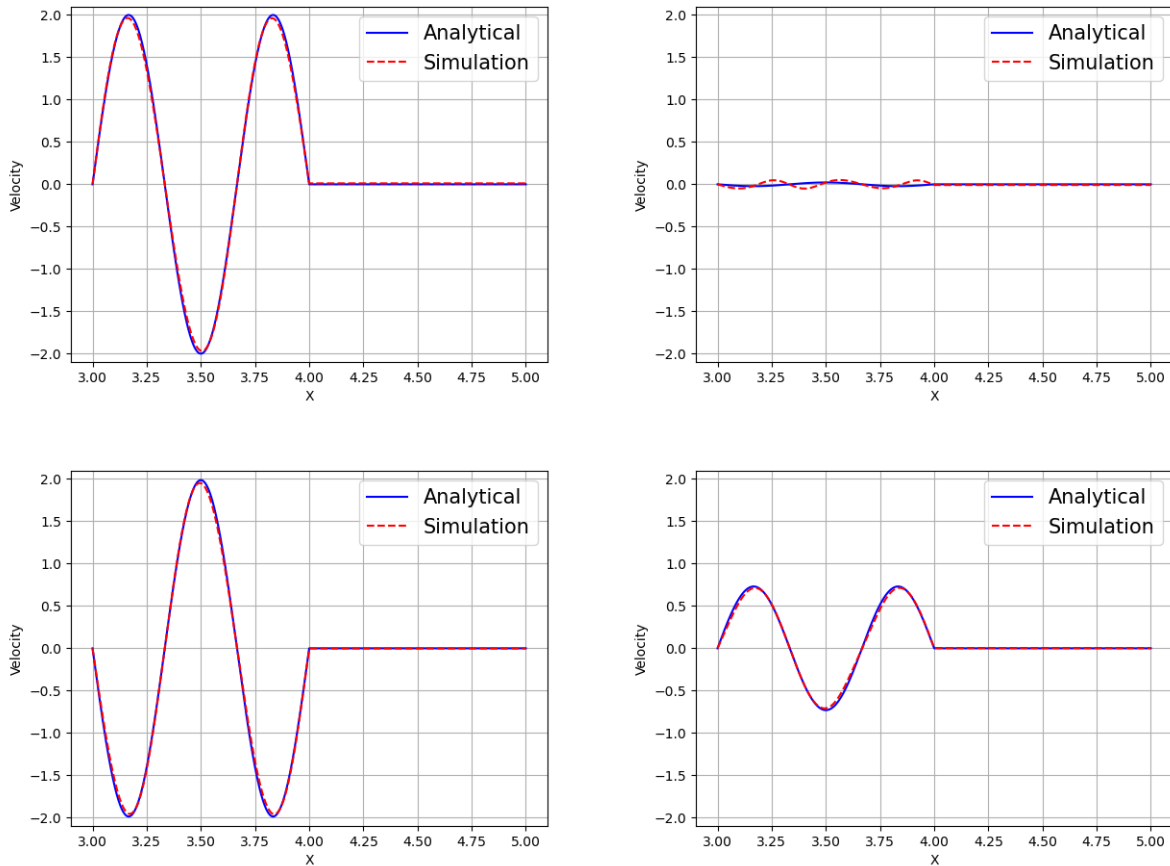


Figure B.11: Velocity profile at different times: $t = 0.43$, $t = 0.425$, $t = 0.475$ and $t = 0.5$ from left to right and top to bottom.

485 *Appendix B.2. Problem II: compressed discs*

A challenging test case can be created simply by setting $R_0 = 1$ in the parameter set outlined in Table 2. As pointed out in Remark 7, a compressed wave propagates in the solid domain, causing the solid mesh to compress and stretch along the radial direction, as shown in Figure B.12. We set $\bar{d} = 0.15$ (5% of the width of the solid domain $R_1 - R_0$) and tested a mesh of 3472 vertices and 7105 triangles, with a time step of 10^{-3} , alongside a remeshing technique to preserve mesh quality. Unfortunately, our simulation breaks down before reaching the maximum displacement at $t = 0.05$.

490

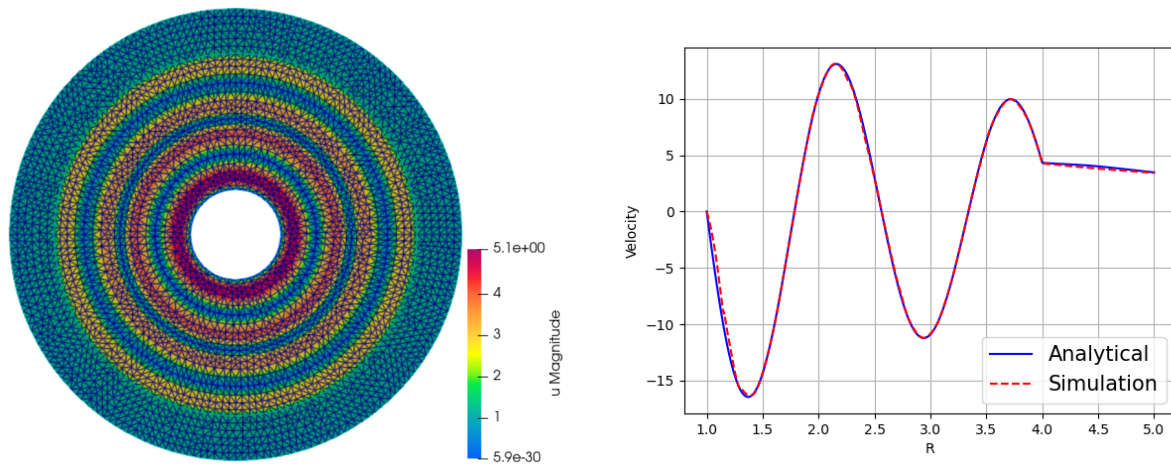


Figure B.12: Velocity magnitude on a 2D mesh (left) and velocity along the radial direction (right) at $t = 0.046$, when $R_0 = 1$ for numerical simulations with multiple compressed waves propagating in the solid. The simulation is run on a mesh of 3472 vertices and 7105 triangles with $\Delta t = 2.5 \times 10^{-4}$.

Appendix B.3. Problem III: rotating discs

To further explore the pressure, we test a simpler case than the one considered in Section 5.5. We use the same parameters as in Table 3, but prescribe a constant angular velocity $\Omega(t) = 0.1$ so that the rotating disc has a steady-state solution. We run the simulation up to $t = 5$ to ensure it reaches a steady-state solution. As shown in Figure B.13, we again observe an inconsistency in the pressure between the 1D and 2D simulations. As the solution approaches the steady state, this inconsistency is only due to a constant shift of the fluid pressure, while the solid pressure agrees well.

References

- [1] C. Farhat, P. Geuzaine, G. Brown, Application of a three-field nonlinear fluid–structure formulation to the prediction of the aeroelastic parameters of an f-16 fighter, *Computers & Fluids* 32 (1) (2003) 3–29.
- [2] Y. Bazilevs, K. Takizawa, T. E. Tezduyar, *Computational fluid-structure interaction: methods and applications*, John Wiley & Sons, 2013.
- [3] Y. Bazilevs, M.-C. Hsu, J. Kiendl, R. Wüchner, K.-U. Bletzinger, 3D simulation of wind turbine rotors at full scale. Part II: Fluid–structure interaction modeling with composite blades, *International Journal for Numerical Methods in Fluids* 65 (1-3) (2011) 236–253.
- [4] Y. Li, A. Castro, T. Sinokrot, W. Prescott, P. Carrica, Coupled multi-body dynamics and CFD for wind turbine simulation including explicit wind turbulence, *Renewable Energy* 76 (2015) 338–361.
- [5] M. Aletti, J.-F. Gerbeau, D. Lombardi, A simplified fluid–structure model for arterial flow. Application to retinal hemodynamics, *Computer Methods in Applied Mechanics and Engineering* 306 (2016) 77–94. doi:10.1016/j.cma.2016.03.044.
- [6] Y. Bazilevs, M.-C. Hsu, Y. Zhang, W. Wang, T. Kvamsdal, S. Hentschel, J. G. Isaksen, Computational vascular fluid–structure interaction: methodology and application to cerebral aneurysms, *Biomechanics and Modeling in Mechanobiology* 9 (4) (2010) 481–498. doi:10.1007/s10237-010-0189-7.
- [7] J. Hron, S. Turek, A monolithic FEM/multigrid solver for an ALE formulation of fluid-structure interaction with applications in biomechanics, *Fluid-structure interaction* (2006) 146–170.
- [8] W. Bai, R. E. Taylor, Fully nonlinear simulation of wave interaction with fixed and floating flared structures, *Ocean Engineering* 36 (3) (2009) 223–236.

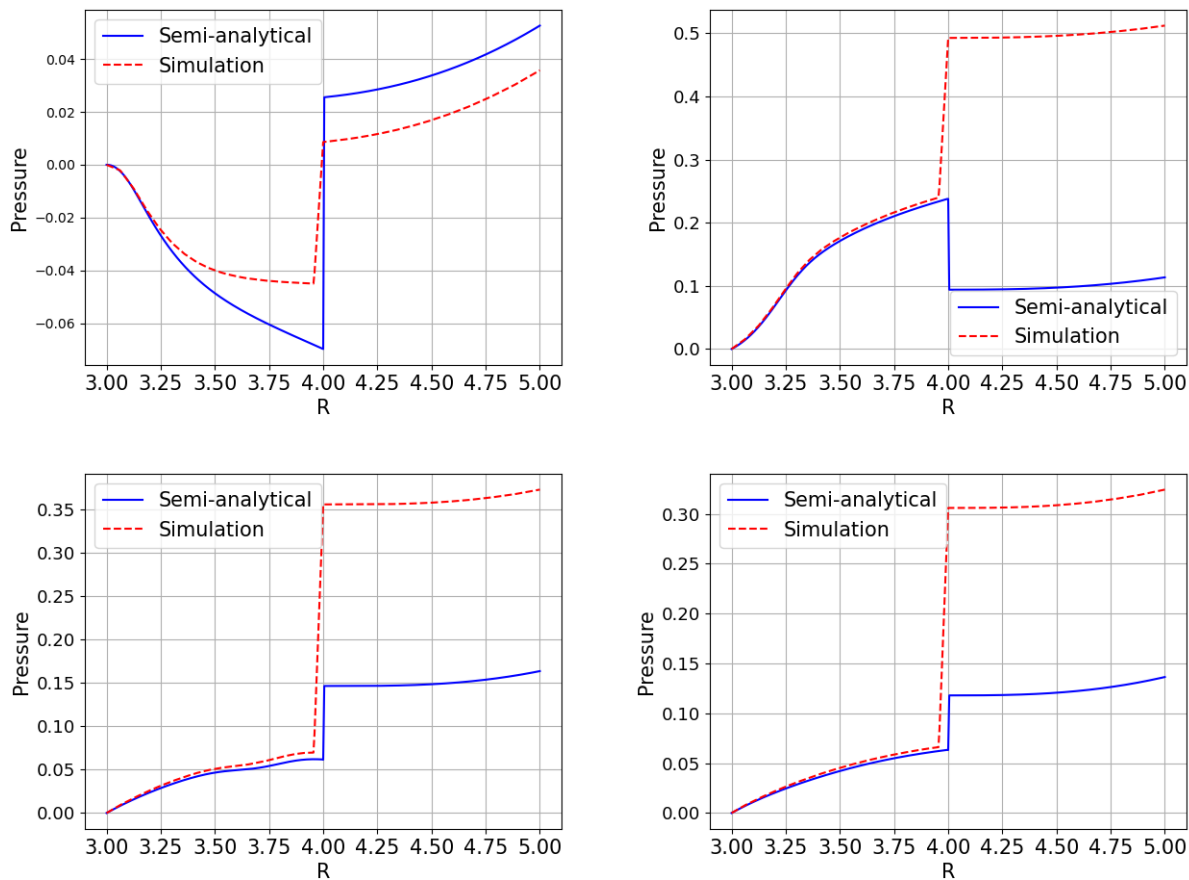


Figure B.13: Pressure of the rotating disc on a medium mesh with $\Delta t = 10^{-3}$ at different times: $t = 0.5$, $t = 1.5$, $t = 2$, and $t = 5$ from left to right and top to bottom. The steady-state solution is reached at $t = 5$.

- [9] W. Finnegan, J. Goggins, Numerical simulation of linear water waves and wave–structure interaction, *Ocean Engineering* 43 (2012) 23–31.
- [10] A. Calderer, X. Guo, L. Shen, F. Sotiropoulos, Coupled fluid-structure interaction simulation of floating offshore wind turbines and waves: a large eddy simulation approach, *Journal of Physics: Conference Series* 524 (2014) 012091. doi:10.1088/1742-6596/524/1/012091.
- 525 [11] A. C. Elias, Fluid-structure interaction simulation of complex floating structures and waves, Ph.D. thesis, University of Minnesota (2015).
- [12] W. A. Wall, D. P. Mok, E. Ramm, Partitioned analysis approach of the transient coupled response of viscous fluids and flexible structures, in: *Solids, Structures and Coupled Problems in Engineering, Proceedings of the European Conference on Computational Mechanics ECCM, Vol. 99, 1999*.
- 530 [13] D. P. Mok, W. Wall, Partitioned analysis schemes for the transient interaction of incompressible flows and nonlinear flexible structures, *Trends in Computational Structural Mechanics, Barcelona*.
- [14] P. Le Tallec, J. Mouro, Fluid structure interaction with large structural displacements, *Computer Methods in Applied Mechanics and Engineering* 190 (24) (2001) 3039–3067.
- 535 [15] H. G. Matthies, J. Steindorf, Partitioned strong coupling algorithms for fluid–structure interaction, *Computers & Structures* 81 (8) (2003) 805–812.
- [16] P. Causin, J.-F. Gerbeau, F. Nobile, Added-mass effect in the design of partitioned algorithms for fluid–structure problems, *Computer Methods in Applied Mechanics and Engineering* 194 (42) (2005)

4506–4527.

- 540 [17] M. Á. Fernández, M. Moubachir, A Newton method using exact Jacobians for solving fluid–structure coupling, *Computers & Structures* 83 (2) (2005) 127–142.
- [18] C. Förster, W. A. Wall, E. Ramm, Artificial added mass instabilities in sequential staggered coupling of nonlinear structures and incompressible viscous flows, *Computer Methods in Applied Mechanics and Engineering* 196 (7) (2007) 1278–1293.
- 545 [19] U. Küttler, W. A. Wall, Fixed-point fluid–structure interaction solvers with dynamic relaxation, *Computational Mechanics* 43 (1) (2008) 61–72. doi:10.1007/s00466-008-0255-5.
- [20] J. Degroote, P. Bruggeman, R. Haelterman, J. Vierendeels, Stability of a coupling technique for partitioned solvers in FSI applications, *Computers & Structures* 86 (23) (2008) 2224–2234.
- [21] U. Küttler, W. A. Wall, Fixed-point fluid–structure interaction solvers with dynamic relaxation, *Computational Mechanics* 43 (1) (2008) 61–72.
- 550 [22] C. Habchi, S. Russeil, D. Bougeard, J.-L. Harion, T. Lemenand, A. Ghanem, D. Della Valle, H. Peerhossaini, Partitioned solver for strongly coupled fluid–structure interaction, *Computers & Fluids* 71 (2013) 306–319.
- [23] J. Degroote, M. Hojjat, E. Stavropoulou, R. Wüchner, K.-U. Bletzinger, Partitioned solution of an unsteady adjoint for strongly coupled fluid–structure interactions and application to parameter identification of a one-dimensional problem, *Structural and Multidisciplinary Optimization* 47 (1) (2013) 77–94.
- 555 [24] T. Yamada, G. Hong, S. Kataoka, S. Yoshimura, Parallel partitioned coupling analysis system for large-scale incompressible viscous fluid–structure interaction problems, *Computers & Fluids* 141 (2016) 259–268.
- 560 [25] R. Haelterman, A. E. Bogaers, K. Scheufele, B. Uekermann, M. Mehl, Improving the performance of the partitioned qn-ils procedure for fluid–structure interaction problems: Filtering, *Computers & Structures* 171 (2016) 9–17.
- [26] S. Basting, A. Quaini, S. Čanić, R. Glowinski, Extended ALE method for fluid–structure interaction problems with large structural displacements, *Journal of Computational Physics* 331 (2017) 312–336.
- 565 [27] T. Spenke, N. Hosters, M. Behr, A multi-vector interface quasi-Newton method with linear complexity for partitioned fluid–structure interaction, *Computer Methods in Applied Mechanics and Engineering* 361 (2020) 112810.
- [28] A. Naseri, A. Totounferoush, I. González, M. Mehl, C. D. Pérez-Segarra, A scalable framework for the partitioned solution of fluid–structure interaction problems, *Computational Mechanics* 66 (2020) 471–489.
- 570 [29] M. Bukač, C. Trenchea, Adaptive, second-order, unconditionally stable partitioned method for fluid–structure interaction, *Computer Methods in Applied Mechanics and Engineering* 393 (2022) 114847.
- [30] M. Bukač, G. Fu, A. Seboldt, C. Trenchea, Time-adaptive partitioned method for fluid–structure interaction problems with thick structures, *Journal of Computational Physics* 473 (2023) 111708.
- 575 [31] F.-K. Benra, H. J. Dohmen, J. Pei, S. Schuster, B. Wan, et al., A comparison of one-way and two-way coupling methods for numerical analysis of fluid–structure interactions, *Journal of Applied Mathematics* 2011.
- [32] N. Hagemeyer, M. Mayr, I. Steinbrecher, A. Popp, One-way coupled fluid–beam interaction: capturing the effect of embedded slender bodies on global fluid flow and vice versa, *Advanced Modeling and Simulation in Engineering Sciences* 9 (1) (2022) 9.
- 580 [33] B. Zou, N. N. B. Thierry, H. Tang, L. Xu, S. Dong, F. Hu, The deformation characteristics and flow field around knotless polyethylene netting based on fluid structure interaction (FSI) one-way coupling, *Aquaculture and Fisheries* 7 (1) (2022) 89–102.
- 585 [34] M. Heil, An efficient solver for the fully coupled solution of large-displacement fluid–structure interaction problems, *Computer Methods in Applied Mechanics and Engineering* 193 (1-2) (2004) 1–23. doi:10.1016/j.cma.2003.09.006.
- [35] B. Hübner, E. Walhorn, D. Dinkler, A monolithic approach to fluid–structure interaction using space–time finite elements, *Computer Methods in Applied Mechanics and Engineering* 193 (23-26) (2004)

- 590 2087–2104.
- [36] M. Heil, A. L. Hazel, J. Boyle, Solvers for large-displacement fluid–structure interaction problems: segregated versus monolithic approaches, *Computational Mechanics* 43 (1) (2008) 91–101. doi:10.1007/s00466-008-0270-6.
- [37] S. Frei, T. Richter, A locally modified parametric finite element method for interface problems, *SIAM Journal on Numerical Analysis* 52 (5) (2014) 2315–2334.
- 595 [38] S. Frei, Eulerian finite element methods for interface problems and fluid-structure interactions, Ph.D. thesis, Universität Heidelberg (2016).
- [39] S. Frei, T. Richter, T. Wick, Locmodfe: Locally modified finite elements for approximating interface problems in deal. ii, *Software Impacts* 8 (2021) 100070.
- 600 [40] E. Burman, M. A. Fernández, S. Frei, F. M. Gerosa, A mechanically consistent model for fluid–structure interactions with contact including seepage, *Computer Methods in Applied Mechanics and Engineering* 392 (2022) 114637.
- [41] E. Burman, P. Hansbo, Edge stabilization for the generalized stokes problem: a continuous interior penalty method, *Computer methods in applied mechanics and engineering* 195 (19-22) (2006) 2393–2410.
- 605 [42] R. L. Muddle, M. Mihajlović, M. Heil, An efficient preconditioner for monolithically-coupled large-displacement fluid–structure interaction problems with pseudo-solid mesh updates, *Journal of Computational Physics* 231 (21) (2012) 7315–7334. doi:10.1016/j.jcp.2012.07.001.
- [43] D. Boffi, L. Gastaldi, A fictitious domain approach with Lagrange multiplier for fluid-structure interactions, *Numerische Mathematik* 135 (3) (2016) 711–732. doi:10.1007/s00211-016-0814-1.
- 610 [44] D. Boffi, N. Cavallini, L. Gastaldi, The finite element immersed boundary method with distributed Lagrange multiplier, *SIAM Journal on Numerical Analysis* 53 (6) (2015) 2584–2604. doi:10.1137/140978399.
- [45] B. Schott, C. Ager, W. A. Wall, A monolithic approach to fluid-structure interaction based on a hybrid Eulerian-ALE fluid domain decomposition involving cut elements, *International Journal for Numerical Methods in Engineering* 119 (3) (2019) 208–237.
- 615 [46] C. Ager, A. Seitz, W. A. Wall, A consistent and versatile computational approach for general fluid-structure-contact interaction problems, *International Journal for Numerical Methods in Engineering* 122 (19) (2021) 5279–5312.
- [47] E. Burman, Ghost penalty, *Comptes Rendus. Mathématique* 348 (21-22) (2010) 1217–1220.
- 620 [48] A. Massing, M. Larson, A. Logg, M. Rognes, A Nitsche-based cut finite element method for a fluid-structure interaction problem, *Communications in Applied Mathematics and Computational Science* 10 (2) (2015) 97–120.
- [49] T. Dunne, R. Rannacher, Adaptive finite element approximation of fluid-structure interaction based on an Eulerian variational formulation, in: *Lecture Notes in Computational Science and Engineering*, Springer Science Business Media, 2006, pp. 110–145. doi:10.1007/3-540-34596-5_6.
- 625 [50] T. Dunne, An Eulerian approach to fluid–structure interaction and goal-oriented mesh adaptation, *International Journal for Numerical Methods in Fluids* 51 (9-10) (2006) 1017–1039. doi:10.1002/flid.1205.
- [51] W. A. Wall, A. Gerstenberger, P. Gamnitzer, C. Forster, E. Ramm, Large deformation fluid-structure interaction-advances in ALE methods and new fixed grid approaches, *Lecture Notes in Computational Science and Engineering* 53 (2006) 195.
- 630 [52] T. Richter, T. Wick, Finite elements for fluid–structure interaction in ALE and fully Eulerian coordinates, *Computer Methods in Applied Mechanics and Engineering* 199 (41-44) (2010) 2633–2642. doi:10.1016/j.cma.2010.04.016.
- 635 [53] R. Rannacher, T. Richter, An adaptive finite element method for fluid-structure interaction problems based on a fully Eulerian formulation, in: *Fluid–Structure Interaction II*, Springer Berlin Heidelberg, 2010, pp. 159–191. doi:10.1007/978-3-642-14206-2_7.
- [54] T. Richter, A fully Eulerian formulation for fluid–structure-interaction problems, *Journal of Computational Physics* 233 (2013) 227–240. doi:10.1016/j.jcp.2012.08.047.
- 640

- [55] T. Wick, Coupling of fully Eulerian and arbitrary Lagrangian–Eulerian methods for fluid–structure interaction computations, *Computational Mechanics* 52 (5) (2013) 1113–1124. doi:10.1007/s00466-013-0866-3.
- [56] O. Pironneau, Numerical study of a monolithic fluid–structure formulation, in: *Variational Analysis and Aerospace Engineering*, Springer International Publishing, 2016, pp. 401–420. doi:10.1007/978-3-319-45680-5_15.
- [57] F. Hecht, O. Pironneau, An energy stable monolithic Eulerian fluid–structure finite element method, *International Journal for Numerical Methods in Fluids* 85 (7) (2017) 430–446. doi:10.1002/flid.4388.
- [58] C.-Y. Chiang, O. Pironneau, T. Sheu, M. Thiriet, Numerical study of a 3D Eulerian monolithic formulation for incompressible fluid–structures systems, *Fluids* 2 (2) (2017) 34. doi:10.3390/fluids2020034.
- [59] Y. Wang, P. K. Jimack, M. A. Walkley, O. Pironneau, An energy stable one-field monolithic arbitrary Lagrangian–Eulerian formulation for fluid–structure interaction, *Journal of Fluids and Structures* 98 (2020) 103117. doi:https://doi.org/10.1016/j.jfluidstructs.2020.103117.
- [60] Y. Wang, P. K. Jimack, M. A. Walkley, A one-field monolithic fictitious domain method for fluid–structure interactions, *Computer Methods in Applied Mechanics and Engineering* 317 (2017) 1146–1168. doi:10.1016/j.cma.2017.01.023.
- [61] Y. Wang, A one-field fictitious domain method for fluid–structure interactions, Ph.D. thesis, University of Leeds (2018).
- [62] Y. Wang, P. K. Jimack, M. A. Walkley, Energy analysis for the one-field fictitious domain method for fluid–structure interactions, *Applied Numerical Mathematics* 140 (2019) 165–182. doi:10.1016/j.apnum.2019.02.003.
- [63] Y. Wang, P. K. Jimack, M. A. Walkley, A theoretical and numerical investigation of a family of immersed finite element methods, *Journal of Fluids and Structures* 91 (2019) 102754.
- [64] G. I. Taylor, Viii. stability of a viscous liquid contained between two rotating cylinders, *Philosophical Transactions of the Royal Society of London. Series A, Containing Papers of a Mathematical or Physical Character* 223 (605-615) (1923) 289–343.
- [65] M. C. Wendl, General solution for the couette flow profile, *Physical Review E* 60 (5) (1999) 6192.
- [66] J. R. Womersley, Method for the calculation of velocity, rate of flow and viscous drag in arteries when the pressure gradient is known, *The Journal of physiology* 127 (3) (1955) 553.
- [67] A. Hesselthaler, M. Balmus, O. Röhrle, D. Nordsletten, A class of analytic solutions for verification and convergence analysis of linear and nonlinear fluid–structure interaction algorithms, *Computer methods in applied mechanics and engineering* 362 (2020) 112841.
- [68] F. Hecht, New development in FreeFem++, *Journal of Numerical Mathematics* 20 (3-4) (2012) 251–265.
- [69] C. Schwartz, Numerical integration of analytic functions, *Journal of Computational Physics* 4 (1) (1969) 19–29.
- [70] U. D. Jentschura, E. Lötstedt, Numerical calculation of bessel, hankel and airy functions, *Computer Physics Communications* 183 (3) (2012) 506–519.
- [71] Ç. Uluişik, L. Sevgi, A tutorial on bessel functions and numerical evaluation of bessel integrals, *IEEE Antennas and Propagation Magazine* 51 (6) (2009) 222–233.
- [72] J. Waldvogel, Towards a general error theory of the trapezoidal rule, *Approximation and Computation: In Honor of Gradimir V. Milovanović* (2011) 267–282.
- [73] C. Schwartz, Numerical calculation of bessel functions, *International Journal of Modern Physics C* 23 (12) (2012) 1250084.
- [74] F. J. Blanco-Silva, *Learning SciPy for numerical and scientific computing*, Packt Pub., 2013.
- [75] L. B. Rall, *Nonlinear functional analysis and applications: proceedings of an advanced seminar conducted by the Mathematics Research Center, the University of Wisconsin, Madison, October 12-14, 1970, no. 26*, Elsevier, 2014.
- [76] D. Boffi, F. Brezzi, M. Fortin, et al., *Mixed finite element methods and applications*, Vol. 44, Springer, 2013.